Doctoral Dissertation

Invention of Silicon Oxide-Based Anode Materials for Rechargeable Batteries

（蓄電池用酸化ケイ素系負極材料の創製）

January 2023

Tomoki Hirono

Department of Chemistry and Biotechnology

Graduated School of Engineering

Tottori University

Preface

The experiments described herein were performed under the guidance of Professor Hiroki Sakaguchi, Associate Professor Hiroyuki Usui, and Associate Professor Yasuhiro Domi at the Applied Chemistry Course, Department of Chemistry and Biotechnology, Graduated School of Engineering, Tottori University between 2020 and 2023.

The goal of this study was to improve the properties of the matrix of next-generation SiO_x-based anode materials and elucidate the mechanism for improving its properties. We believe that the findings of our experiments will promote the development of storage batteries with high energy density.

Tomoki Hirono

Department of Chemistry and Biotechnology

Graduate School of Engineering

Tottori University

4-101 Minami, Koyama-cho, Tottori 680-8552, Japan

January 2023

Content

General Introduction

Currently, global warming is a growing concern owing to the increase in the amount of emitted greenhouse gases worldwide. Since the Industrial Revolution, humankind has continued to mass-produce and consume goods in an ongoing quest for affluence. Consequently, the amount of emitted greenhouse gases has increased gradually and global warming progressed. Therefore, countries worldwide are devoting considerable efforts to building a low-carbon society and decreasing greenhouse gas emission. In this context, storage batteries are critical devices of modern society.

Storage batteries are expected to be used as electric batteries for automobiles and emergency power sources. It is also anticipated that storage batteries store renewable energy and serve as backup power sources, as devices that can adjust power supply and demand, and for communication base stations. In particular, the recent expansion of the electric vehicle and other markets led to the rapid progress of in-vehicle batteries.

Li-ion batteries, which are a common type of secondary batteries, store renewable energy and can be used repeatedly without emitting CO_2, thereby contributing to the development of a low-carbon society. Furthermore, Li-ion batteries have attracted increasing attention as devices that can promote achievement of a sustainable society, because they does not contain Cd or Pb and their environmental load is small. In addition, the electromotive force of Li-ion batteries is high (~4 V). Therefore, recently, Li-ion batteries have been used in

to power a wide variety of devices, such as wearable devices, drones, and electric vehicles, and it is expected that they will be used in aircrafts in the future.

Graphite is a commonly used anode material with an initial capacity reversibility of > 90 %. In addition, graphite presents excellent cycle properties, because its volume change during charge–discharge is small. However, the theoretical capacity of graphite is only 372 mA h g^{-1}, and the experimental capacity of graphite cannot exceed the theoretical capacity.

Therefore, Si has captured the interest of researchers as an attractive active anode material for Li-ion batteries, because it belongs to the same group of the periodic table as C (group 14) and can be repeatedly and reversibly alloyed and dealloyed with Li-ions. Si is a critical material for increasing the capacity of Li-ion batteries, because its theoretical capacity (3600 mA h g^{-1}) is ~10 times higher than that of graphite. However, Si cannot be smoothly alloyed and dealloyed with Li-ions because the electron conductivity of Si is low and the diffusion of Li-ions is slow. Moreover, the volume change of Si during lithiation and delithiation reaches ~380 %, and the stress generated during lithiation and delithiation causes cracks in Si particles, which fall from the current collector. Consequently, capacity decreases rapidly, because the contact between the active material surrounding Si particles and conductive material is interrupted and the Si particles become electrically isolated and cannot participate in subsequent charge–discharge reactions.

Several researchers have examined this issue.[1–15] In particular, SiO_x-based materials,

such as those used as anode materials for electric vehicles, have recently attracted increasing attention. We have previously demonstrated that SiO_x comprises a mixture of Si and SiO_2 phases, and the structure of nanosized clustered Si consists of Si particles finely dispersed in a SiO_4 tetrahedral matrix.[16] Because the cycle properties of the SiO_2 matrix are superior to those of pure Si, SiO_x can relieve the stress induced by volume expansion during charging–discharging.[17]

However, the decrease in the capacity of SiO_x during charging–discharging is significantly higher than that of graphite. This is because the reaction of SiO_x with Li-ions occurs locally owing to the low electronic conductivity of SiO_x, and that part becomes the starting point, cracks form, and then the electrode disintegrates. Therefore, SiO_x and graphite mixtures have been used as anode materials for electric vehicles. In the future, the SiO_x-to-graphite mixing ratio should be adjusted to extend battery life and increase the driving range of electric vehicles. Furthermore, the properties of SiO_x-based anode materials should be improved.

Numerous studies have been conducted on SiO_x-based anode materials.[18–22] For example, an activated graphene/porous Si@SiO_x composite[23] and core–shell Si–SiO_x nanocomposites,[24,25] which provided ample space for the volume expansion and contraction of Si during charging–discharging, were used as anodes for Li-ion batteries. Moreover, SiO_x was mixed with carbon to improve the electrical conductivity of SiO_x-based anode

materials.[26] Alternatively, researchers have devoted considerable efforts to improving the reactivity of SiO_x by promoting the formation of suboxide-type tetrahedra, such as Si-(3Si, O), Si-(2Si, 2O), Si-(Si, 3O) at the Si–SiO_2 interface.[27] However, to the best of our knowledge, to date no studies focused on improving the properties of the SiO_2 matrix.

Conventional SiO_x manufacturing methods involve mixing Si and SiO_2, heating and then cooling the mixture, precipitating the generated SiO gas, and lastly precipitating fine Si particles via a disproportionation reaction ($2SiO \rightarrow Si + SiO_2$).[28] However, it is challenging to control the Si content of SiO_x because the boiling point of Si (3538 K) is considerably higher than that of SiO (2153 K). In addition, the precise addition of elements with different boiling points to SiO_x matrices is challenging.

Therefore, in this study, we used a mechanical milling (MM) method to fabricate SiO_x-based materials because it facilitated the addition of materials and did not involve a gas-phase reaction. The electronic conductivity of the SiO_x-based anode materials fabricated via MM was higher than that of the SiO_2 matrix; moreover, the MM method allowed us to manufacture samples with various material designs.

This thesis is structured as follows.

Chapter 1: We evaluated the charge–discharge properties of *M*/SiO_x (*M* = Al, B, and Sn) anode materials for Li-ion secondary batteries. First, SiO_x was prepared via MM, and then the effect of the addition of a third element (*M*) on the properties of the anode materials was

investigated.

Chapter 2: We analyzed the effect of the amount of Sn on the properties of Sn/SiO_x anode materials with remarkable properties to improve their cycle life.

Chapter 3: We evaluated the possibility of using Sn/SiO_x as anode materials for Na-ion batteries and the effects of Sn loading on the anode properties.

Lastly, we present our concluding remarks.

Chapter 1

Improvement of the Anode Properties of Lithium-Ion Batteries for SiO_x with a Third Element

1.1 Introduction

Li-ion batteries have been used as power sources for many types of devices, such for laptop computers, because they are lighter and have higher energy density than other secondary batteries. Recently, the demand for batteries with high energy density has increased owing to the increasing performance demands of portable electronic devices and development of electric vehicles. Therefore, cathode and anode materials with high capacity should be developed.

Graphite is commonly used as an anode material, and its initial capacity reversibility has exceeded 90 %. In addition, graphite presents excellent cycle properties because its volume change during charging–discharging is small. However, the theoretical capacity of graphite is only 372 mA h g^{-1}, and the experimental capacity of graphite is not expected to exceed the theoretical capacity.

Therefore, Si is an attractive active anode material for Li-ion batteries because Si and C belong to the same group of the periodic table, and Si can be repeatedly and reversibly alloyed and dealloyed with Li-ions. Si is a critical material for fabricating high-capacity

Li-ion batteries because its theoretical capacity (3600 mA h g^{-1}) is ~10 times higher than that of graphite. However, Si cannot smoothly alloy and dealloy with Li-ions because its electron conductivity is low and the diffusion of Li-ions is slow. Additionally, Si undergoes large volume changes of ~380 % during lithiation–delithiation, and the stress generated during lithiation–delithiation induces cracks in Si particles, causing the particles to fall from the current collector. Consequently, anode capacity decreases rapidly because the contact between the active material, surrounding Si particles, and conductive material is interrupted. This causes the Si particles to become electrically isolated, and therefore, they cannot participate in subsequent charge–discharge reactions.

Various approaches have been used to mitigate this shortcoming.[2–5,7–10,14,15,29–38] For example, for Li-ion batteries fabricated using small Si crystallites (≤ 10 nm), the yield stress exceeded the stress generated during charging; consequently, cracking of Si particles was suppressed and the cycle properties of the anode materials were improved. In addition, cracking of Si particles was suppressed and the cycle properties of Si-based anode materials were improved by decreasing the size of Si particles to ≤ 150 nm.[39]

Owing to various developments, SiO_x has recently been used as the anode material of Li-ion batteries for electric vehicles with long driving range. This was ascribed to the capacity of SiO_x being higher than that of graphite.

SiO_x comprises a mixture of Si and SiO_2 phases. Our research group has previously demonstrated that SiO_x is an amorphous material comprising a three-dimensional SiO_4 tetrahedral network similar to that of silica (SiO_2) glass with embedded metallic Si clusters, and Si clusters were finely dispersed throughout the SiO_4 matrix.[16] The cycle properties of SiO_2 matrices are superior to those of Si because the SiO_4 matrix relaxes the stress induced by the volume expansion of Si during charging–discharging.[17]

However, the decrease in capacity of SiO_x during charging–discharging is significantly higher than that of graphite. This was attributed to the reaction of SiO_x with Li-ions being localized owing to the poor electron conductivity of SiO_x and cracking of the active material causing the electrode to collapse. Therefore, SiO_x has been mixed with graphite to fabricate anode materials for the Li-ion batteries of electric vehicles. In the future, it is expected that the SiO_x-to-graphite mixing ratio will be increased to extend the life of Li-ion batteries and further increases the driving range of electric vehicles. Moreover, the properties of SiO_x-based anode materials should be improved.

The primary efforts toward improving the properties of SiO_x-based anode materials have involved improving Si particles and increasing conductivity. To the best of our knowledge, no studies have focused on the SiO_2 amorphous matrix or addition of a third element to SiO_2 matrices to improve their properties. Therefore, we developed a new method

for improving the properties of SiO_x-based anode materials by increasing the low electronic conductivity of the SiO_2 matrix.

Figure 1-1 shows a schematic of the SiO_x structure.[16] Conventional SiO_x comprises cluster-shaped Si dispersed throughout a SiO_2 matrix with a SiO_4 tetrahedral network structure. However, SiO_2 is an insulator, and its electron conductivity is low (10^{-18} S cm^{-1}). Therefore, a third element (*M* = Al, B, and Sn) was added to the SiO_4 tetrahedral network structure. This was expected to increase the electron conductivity of the SiO_2 matrix and promote the uniform reaction of Li-ions with the SiO_x-based electrode material. Therefore, we considered that the damage to the electrodes was negligible and electrode collapse was suppressed, because the stress induced by the volume expansion of Si during charging–discharging could not accumulate.

Conventional SiO_x is manufactured by mixing Si and SiO_2, heating then cooling the mixture, precipitating the SiO gas generated, and precipitating fine Si through a disproportionation reaction ($2SiO \rightarrow Si + SiO_2$).[28] However, controlling the Si content of SiO_x is challenging because the boiling point of Si (3538 K) is significantly higher than that of SiO (2153 K). In addition, it is challenging to precisely add elements with different boiling points to SiO_x. Therefore, we used an MM method to fabricate SiO_x-based materials because it favored the addition of elements, and it did not involve a gas phase. In this study, we evaluated the charge–discharge properties of *M*/SiO_x (*M* = Al, B, and Sn) anode materials for

Li-ion batteries prepared using MM and investigated the effect of the addition of *M* (Al, B, and Sn) on the properties of the anode materials.

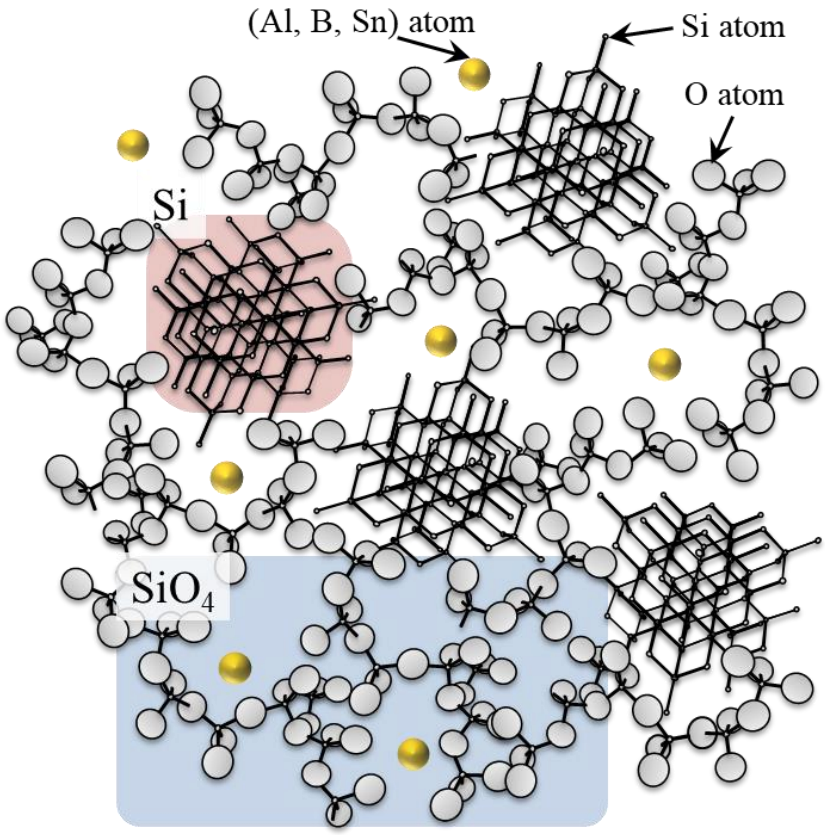

Figure 1-1. Schematic of the SiO_x structure.

1.2 Experimental

1.2.1 Sample preparation

1.2.1.1 Preparation of SiO_x and M/SiO_x (M = Al, B, and Sn) powders

Si powder was prepared using a commercially available gas-atomizing device (Figure 1-2). Flake-shaped Si raw particles (purity 98.7 %, size ~10–20 mm) were added to a crucible

with Φ2.5 mm pores at the bottom and melted under a dry Ar gas atmosphere in a high-frequency induction melting furnace. The molten metal was then discharged at 1823 K, N_2 gas was sprayed onto the molten metal directly below the bottom of the crucible, and then the metal was solidified at a cooling rate of ~$10^{0\text{-}2}$ K s^{-1}. The as-obtained gas-atomized Si powder was screened using a 300 μm sieve (Figure 1-3).

To prepare SiO_x powder, a mixture of gas-atomized Si powder (32.4 g) and commercially available SiO_2 powder (27.6 g; purity 99.9 %; Kojundo Chemical Lab. Co., Ltd.) was placed in an austenite-based stainless-steel vessel containing Φ19 mm high-carbon chromium bearing steel (C 1 %, Cr 1 %) balls with the total mass of 12 kg. The Si:SiO_2 mass ratio was 54:46, and the active-material–to–balls mass ratio was 1:200.

To prepare *M*/SiO_x (*M* = Al, B, and Sn) powders, we used Al (purity 99.9 %) B (purity 99.9 %), and Sn (purity 99.0 %) purchased from Kojundo Chemical Lab. Co., Ltd.. In brief, mixtures of gas-atomized Si powder (31.4 g), commercially available SiO_2 powder (26.8 g), and *M* (Al, B, and Sn) powder (1.8 g) were placed in austenite-based stainless-steel vessels containing high-carbon chromium bearing steel balls with the total mass of 12 kg such that the Si:SiO_2:*M* mass ratio was 52:45:3. The vessels were sealed, the interior was evacuated to a pressure of 0.1 MPa, and dry Ar gas was introduced through gas replacement. Thereafter, the vessels were placed in a vibrating ball mill (MB-1, Chuo Kakohki Co., Ltd.). After 14 h of MM at an amplitude of ± 4 mm and a frequency of 1200 rpm, the number of steel balls

was increased such that the active-material–to–balls mass ratio was 1:300, and MM was continued for 14 h (Figure 1-4).

The particle size of the as-obtained powders was adjusted to ≤ 10 μm owing to collisions between powder particles under a 0.7 MPa N_2 gas stream using a jet mill (Co-Jet, Seishin Enterprise Co., Ltd.) to crush the agglomerated powders and obtain the target powders.

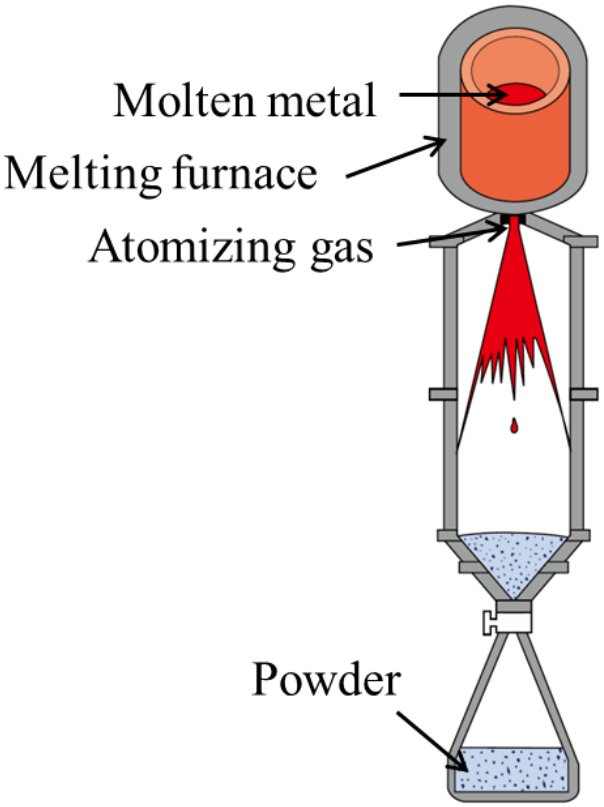

Figure 1-2. Schematic of the gas atomizer.

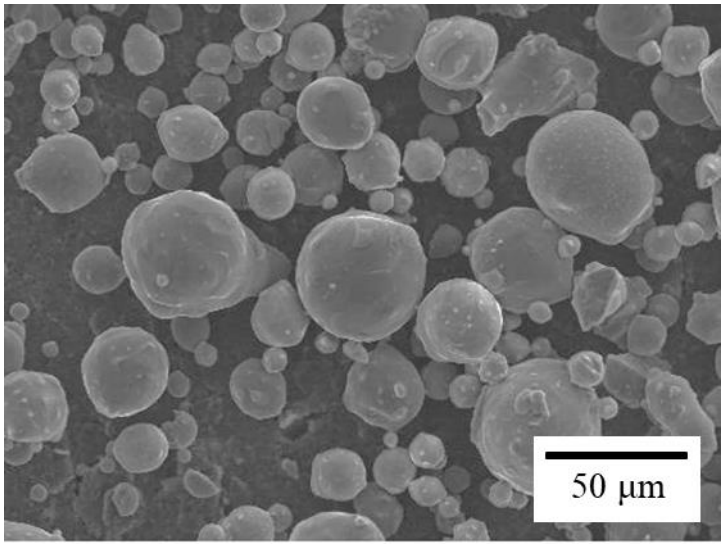

Figure 1-3. SEM image of gas-atomized Si powder.

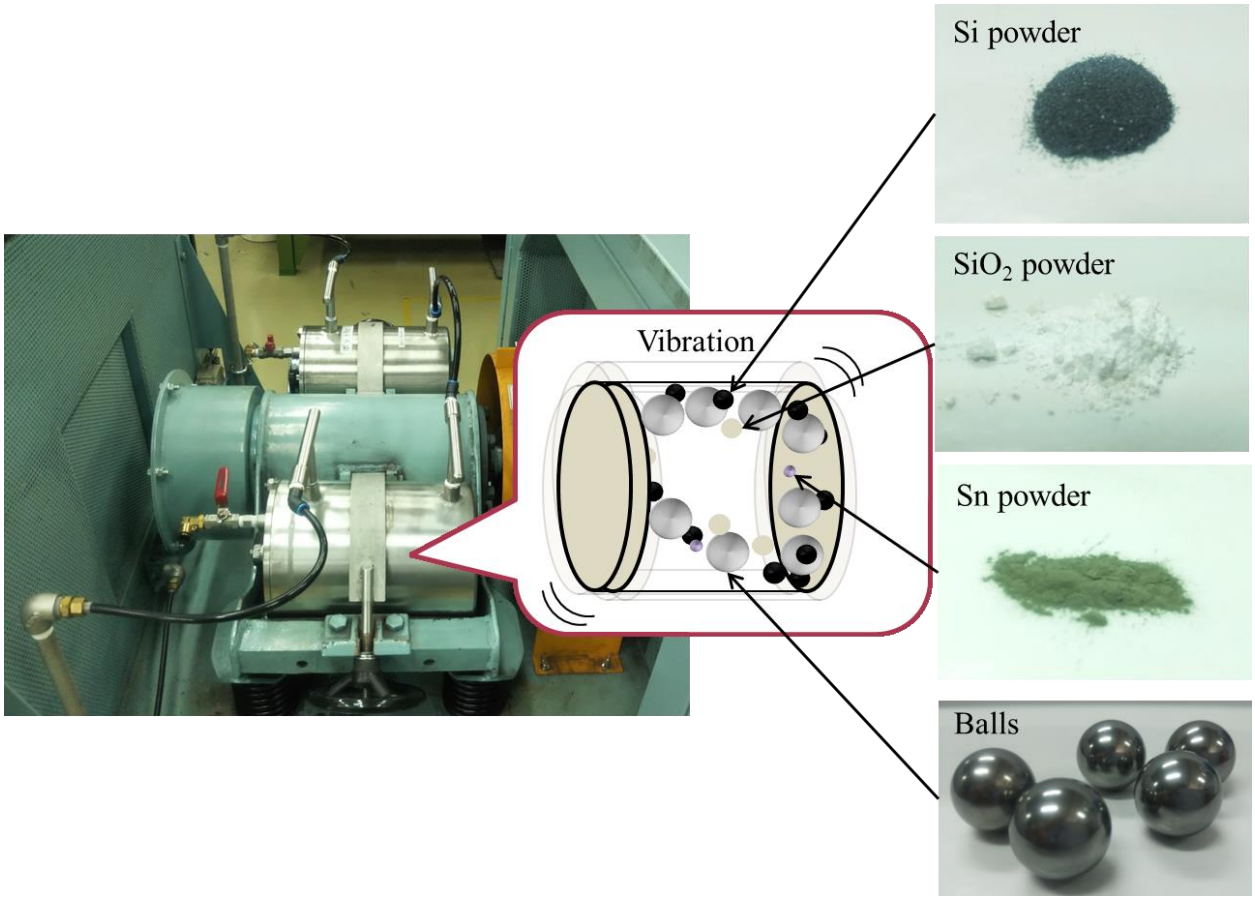

Figure 1-4. Photograph and schematic diagram of the vibrating ball mill. Photographs of raw Si, SiO_2, and Sn powders and high-carbon chromium steel balls used to fabricate Sn/SiO_x powder.

1.2.1.2 Preparation of *M*/SiO_2 (*M* = Al, B, and Sn) and SiO_2 powders

For comparison, *M*/SiO_2 (*M* = Al, B, and Sn) powders were fabricated using the same procedure by mixing SiO_2 with *M* (Al, B, and Sn) in the absence of gas-atomized Si powder. The changes in the properties (reactivity with Li-ions) of the SiO_2 matrix owing to the presence of the third element *M* (Al, B, and Sn) were investigated.

To prepare *M*/SiO_2 (*M* = Al, B, and Sn) powders, we used Al (purity 99.9 %) and B (purity 99.0 %) purchased from FUJIFILM Wako Pure Chemical Corporation, and Sn (purity 99.9 %, 325 mesh) acquired from Rare Metallic Co., Ltd. In brief, commercially available SiO_2 powder and *M* (Al, B, and Sn) powders (total powder mass of 1.5 g) were weighed and placed in zirconia vessels containing Φ5 mm zirconia balls with a total mass of 100 g such that the SiO_2:*M* (Al, B, and Sn) mass ratio was 94:6. The vessels were sealed and placed in a PL-7 premium line planetary ball mill. The powders were subjected to MM for various times (SiO_2: 20 h, Al/SiO_2: 40 h, B/SiO_2: 20 h, and Sn/SiO_2: 20 h) at 380 rpm to obtain the target powders.

1.2.2 Analysis of the as-fabricated SiO_x and *M*/SiO_x (*M* = Al, B, and Sn) samples

The Si crystallite sizes of the SiO_x and *M*/SiO_x (*M* = Al, B, and Sn) powders were

measured using an X-ray diffraction (XRD; RINT-2500, Rigaku) instrument with Cu Kα radiation operated at 50 kV and 200 mA, at a scanning rate of 4° min^{-1}, and in the scanning range of 20–60°.

The morphologies of the powders were observed using a scanning electron microscopy (SEM; JSM-6490LV, EOL Ltd.) device operated at 5 kV. Samples of the prepared powders were attached to conductive tape for observation.

The size and dispersibility of nanocrystalline Si and *M* (Al, B, and Sn) were observed using a transmission electron microscopy (TEM; JEM-F200, JEOL Ltd.) apparatus operated at 200 kV. Prior to observation, the samples were prepared as follows. First, samples of the prepared powders were embedded in a conductive thermosetting resin. Subsequently, a carbon protective film was deposited on the surface of each sample. Lastly, the samples were cut into 10 μm × 10 μm × 100 nm specimens using a high-performance focused ion beam device (MI4050, Mo mesh, Hitachi High-Tech Corporation).

The electron conductivity of the obtained powders was evaluated using a powder resistivity measuring unit (MCP-PD51, Nittoseiko Analytech Co., Ltd.) with four probes. Prepared powder (~3 g) was placed in a sample holder Φ10 mm and compressed under a maximum pressure of 64 MPa to measure the volumetric electronic conductivity of each sample (Figure 1-5).

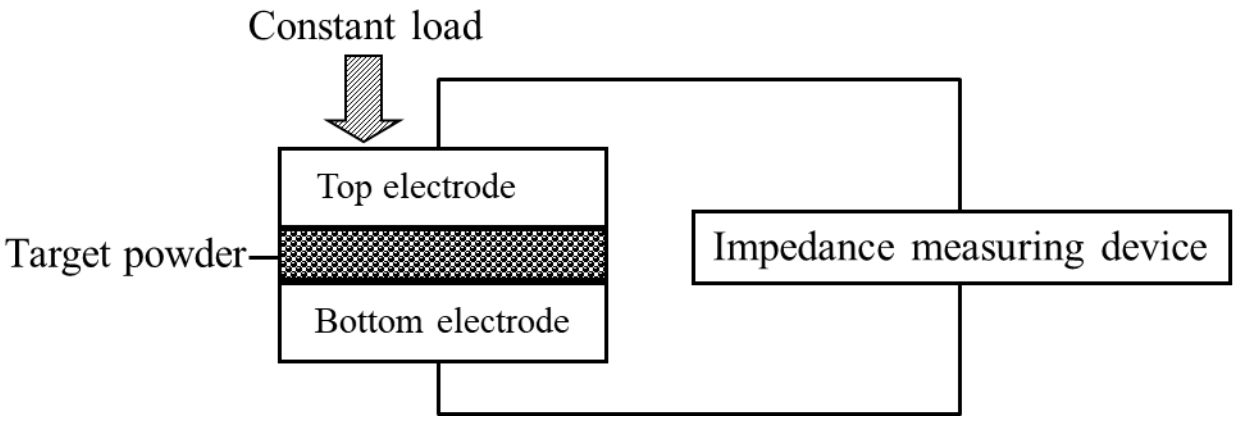

Figure 1-5. Schematic of the system used to measure the volumetric electronic conductivity of the target powders.

1.2.3 Electrode fabrication

SiO_x, M/SiO_x, SiO_2, and M/SiO_2 (M = Al, B, and Sn) powders were individually mixed with acetylene black, carboxymethyl cellulose, and styrene–butadiene rubber at mass ratios of 70:15:10:5 using a kneading machine. Cu films were then deposited onto the surface of the samples (coating mass per unit of surface area of ~1.0 mg cm^{-2}) to fabricate electrodes (Figure 1-6).

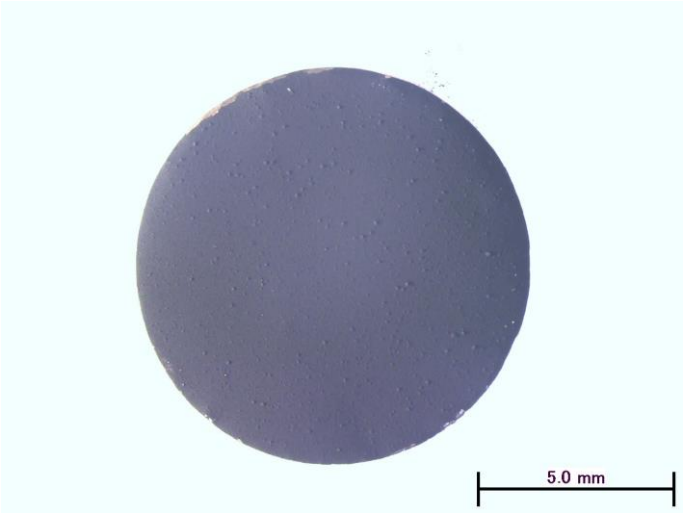

Figure 1-6. Photograph of a fabricated SiO_x electrode as an example.

1.2.4 Cell assembly and charge–discharge tests

Several 2032-type coin cells comprising SiO_x, *M*/SiO_x, SiO_2, or *M*/SiO_2 (*M* = Al, B, and Sn) electrodes as the working electrode, a Li metal sheet as the counter electrode, and a glass fiber filter as the separator were assembled and used for charge–discharge tests. A 1 M solution of lithium bis(trifluoromethanesulfonyl)amide (LiTFSA) in propylene carbonate (PC) was used as the electrolyte. Cell assembly and electrolyte preparation were conducted in an Ar-filled glovebox (DBO-2.5LNKP-TS, Miwa Mfg. Co. Ltd.) with an O_2 content < 1 ppm and a dew point < 173 K (Figure 1-7). Moreover, we demonstrated that this material can be used in cold climates. Therefore, we evaluated its performance using PC (melting point (MP) = 223 K) with a lower melting point than ethylene carbonate (MP = 311 K) and is difficult to freeze.

The SiO_x and M/SiO_x (M = Al, B, and Sn) electrodes were subjected to galvanostatic charge–discharge cycling tests using an electrochemical measurement system in the potential range of 0.005–2.000 V vs. Li^+/Li. The current density and measurement temperature were set to 1.60–1.93 A g^{-1} (1 C) and 303 K, respectively. Electrochemical measurements were performed using a charge limit of 1000 mA h g^{-1}. In this study, we considered that SiO_x comprised a mixture of Si and SiO_2, and SiO_2 was inactive toward Li-ions. Therefore, the theoretical capacitance was calculated assuming that only Si reacted with Li-ions. The maximum alloying composition was calculated to be $Li_{15}Si_4$. The theoretical capacities of SiO_x, Al/SiO_x. B/SiO_x, and Sn/SiO_x were calculated to be 1931, 1890, 1860, and 1890 mA h g^{-1}, respectively. The galvanostatic charge–discharge tests for the SiO_2 and M/SiO_2 (M = Al, B, and Sn) electrodes were performed in the potential range of 0.005–2.000 V vs. Li^+/Li at a current density of 0.38 A g^{-1} and measurement temperature of 303 K.

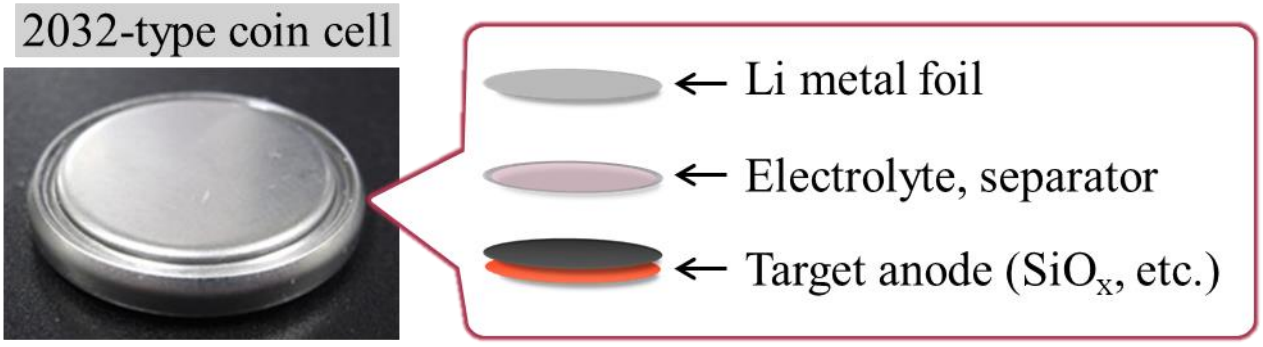

Figure 1-7. Schematic of a 2032-type coin cell used for charge–discharge tests.

1.3 Results and Discussion

1.3.1 Shape of powder particles

Figure 1-8 shows the SEM images of the as-prepared SiO_x and M/SiO_x (M = Al, B, and Sn) powders. Secondary particles with a size of ~5 μm and irregular shapes were present in all samples. Therefore, it was concluded that the effect of the third element on the size and shape of the secondary particles was negligible. However, the shape of the primary particles could not be confirmed. Therefore, the primary particles were expected to present mixed shapes and sizes smaller than several hundred nanometers.

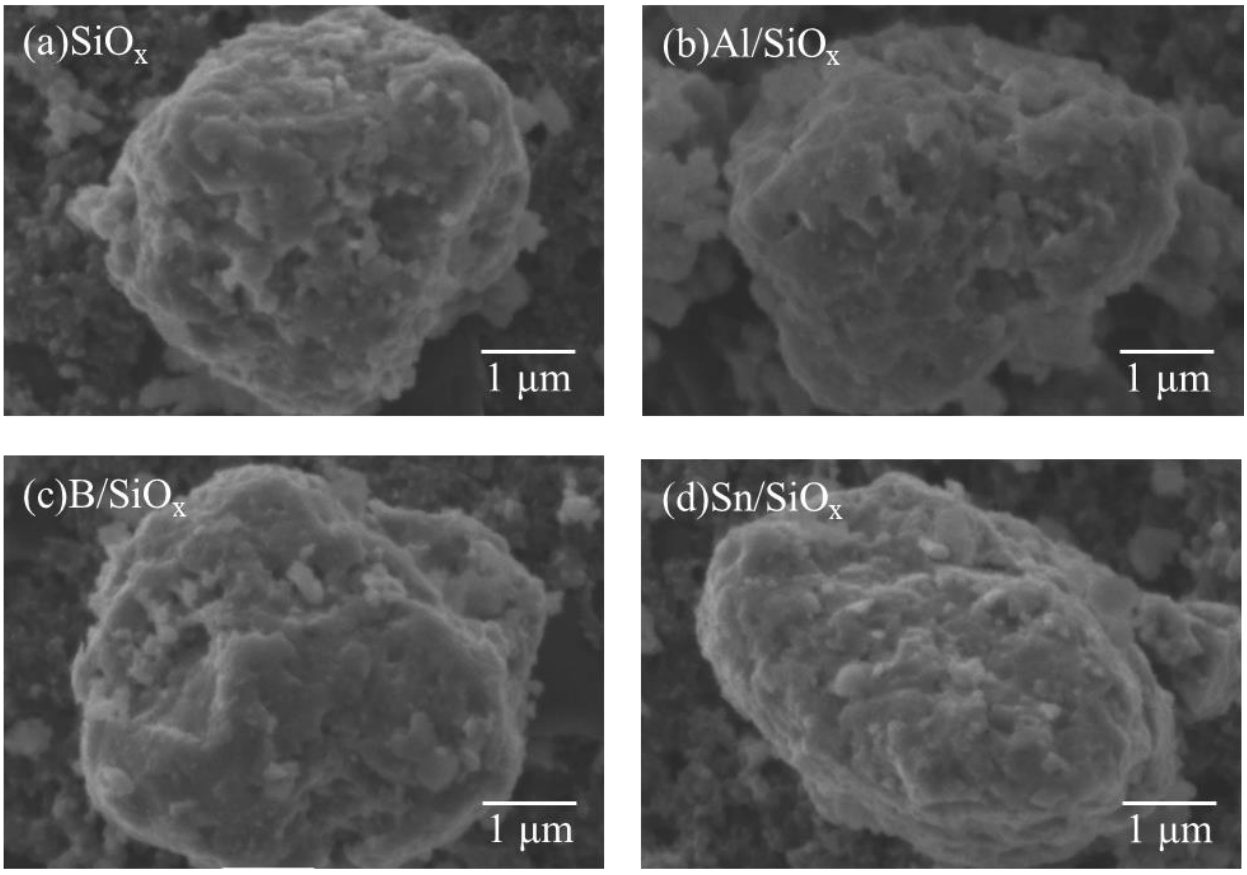

Figure 1-8. SEM images of milled SiO_x and M/SiO_x (M = Al, B, and Sn) powders.

1.3.2 Structure of powders

It was anticipated that the raw material powders would react with Si or that the third element would dissolve in Si because of the high energy generated during ball collision inside the vibrating ball mill. First, we evaluated the structures of the prepared target materials (Figure 1-8). The SEM images revealed that SiO_x powder comprised cluster-shaped Si dispersed throughout a SiO_2 matrix, whereas the M/SiO_x (M = Al, B, and Sn) powders comprised cluster-shaped Si and M (Al, B, and Sn) particles dispersed throughout SiO_2

matrices.

The characteristic peaks of Si at (111), (220), and (311) were present in the XRD patterns of the as-prepared SiO_x and *M*/SiO_x (*M* = Al, B, and Sn) powders (Figure 1-9(a)). The Si crystallite size for the as-prepared SiO_x and *M*/SiO_x (*M* = Al, B, and Sn) powders was calculated to be ~8–12 nm using the Scherrer's equation. However, the characteristic peak of SiO_2 was not present in the XRD patterns of the as-prepared SiO_x and *M*/SiO_x (*M* = Al, B, and Sn) powders. This was attributed to SiO_2 becoming amorphous-like owing to the high energy during MM.

The presence of the characteristic peaks of Al, B, Sn and their compounds, such as oxides, in the XRD patterns of the as-prepared *M*/SiO_x (*M* = Al, B, and Sn) powders was not confirmed. Moreover, we used the position of the Si diffraction peak at ~28°, which corresponded to the (111) plane of Si, to evaluate whether the third element was dissolved in Si or dispersed throughout the SiO_2 matrix. Figure 1-9(b) shows the XRD patterns of the SiO_x and *M*/SiO_x (*M* = Al, B, and Sn) powders in the 2θ range of 25–32°. The crystal lattice of Si should expand or contract upon dissolution of the third element in Si, and the characteristic diffraction peak of Si should down- or upshift, respectively.[40] However, the position of the characteristic peak of Si at ~28° in the XRD patterns of the as-prepared SiO_x and *M*/SiO_x (*M* = Al, B, and Sn) powders was the same. Therefore, we demonstrated that the third element was not dissolved in Si, instead it became amorphous and was dispersed throughout the SiO_2

matrix, as intended.

These results confirmed that the as-prepared M/SiO_x (M = Al, B, and Sn) powders comprised amorphous-like SiO_2 and nanocrystalline Si, and the third element was not dissolved in Si.

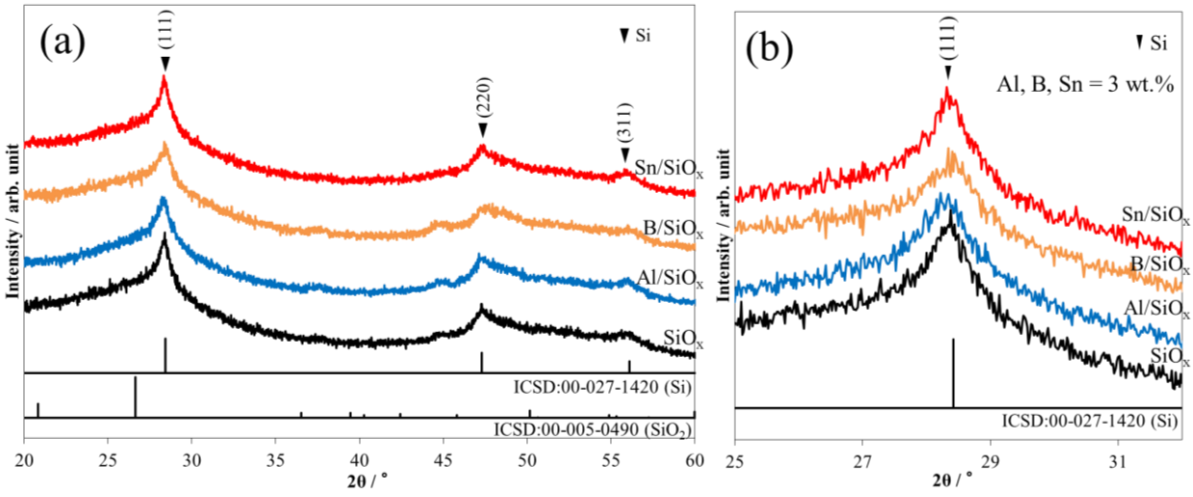

Figure 1-9. XRD of the as-prepared SiO_x and M/SiO_x (M = Al, B, and Sn) powders in the 2θ ranges of (a) 20−60° and (b) 25−32°.

Subsequently, the structures of the as-prepared SiO_x and M/SiO_x (M = Al, B, and Sn) powders were analyzed. Figure 1-10(a) shows a low-magnification bright-field TEM image of the edge of SiO_x particles. The black spots and gray areas are Si particles and the SiO_2 matrix, respectively. The TEM image revealed that Si and SiO_2 were finely pulverized after MM, and Si formed a dispersed structures throughout the SiO_2 matrix. Figure 1-10(b) shows the high-resolution bright-field TEM image and electron diffraction patterns of SiO_x powder.

Most of the gray areas, except for the black spots, presented halo patterns. It was considered that the gray areas were amorphous SiO_x because energy-dispersion X-ray spectroscopy (EDS) data demonstrated that they comprised 78 wt.% Si and 22 wt.% O_2. Conversely, the black spot encircled with a red dashed line (1) was confirmed to be elemental Si using electron diffraction analysis. Moreover, the size of Si microcrystals was determined to be ~10 nm. These results indicate that fine Si particles were dispersed throughout an amorphous SiO_2 matrix, as predicted using XRD data.

Similarly, we determined that the black spots encircled with red dashed lines in the high-resolution TEM images of the Al/SiO_x and Sn/SiO_x powders ((2) and (3) in Figure 1-10(c) and (d), respectively) comprised elemental Si using electron diffraction patterns; moreover, the particle size of Si was ~10 nm. Furthermore, the amorphous SiO_2 matrices of the Al/SiO_x and Sn/SiO_x powders were different from that of the SiO_x powder. EDS analysis revealed that the Al/SiO_x powder comprised 73 wt.% Si, 24 wt.% O, and 1.8 wt.% Al, whereas the Sn/SiO_x powder comprised 72 wt.% Si, 23 wt.% O, and 2.1 wt.% Sn. These results further confirmed that the third element was dispersed throughout the amorphous SiO_2 matrices of M/SiO_x (M = Al, B, and Sn).

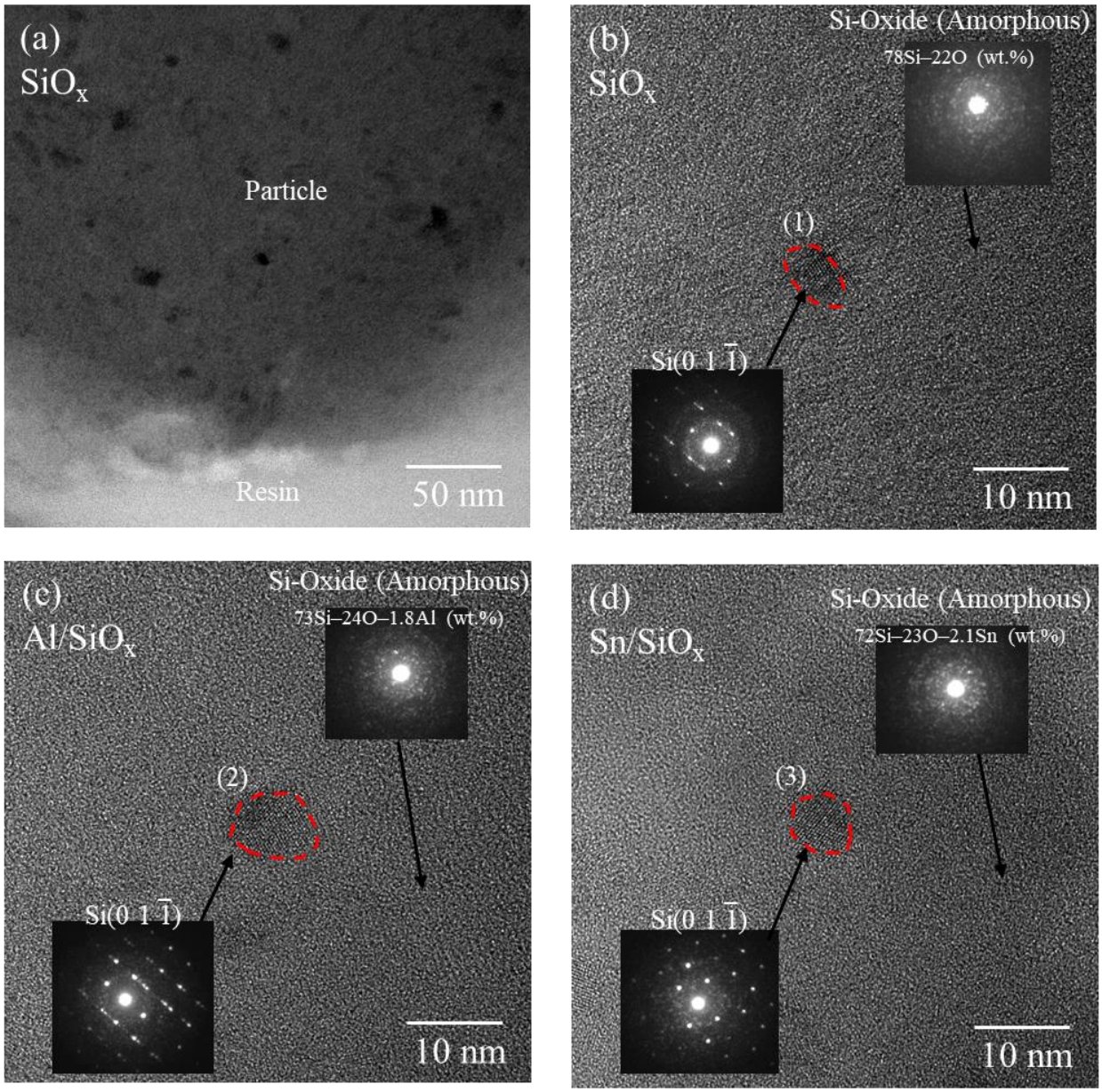

Figure 1-10. (a) Low- and (b) high-resolution TEM images of an as-prepared SiO_x particle High-resolution TEM images of (c) Al/SiO_x and (d) Sn/SiO_x particles. Electron diffraction patterns of SiO_x (top) and Si (bottom) in the insets of (b)–(d).

The distribution of the third element was confirmed using the bright-field TEM images and Al, B, and Sn EDS mappings of *M*/SiO_x (*M* = Al, B, and Sn) particles (Figure 1-11). Al and Sn were not present within the Si microcrystals of Al/SiO_x and Sn/SiO_x powders,

respectively; instead they were uniformly dispersed throughout the SiO_x matrices. Furthermore, B was dispersed throughout the SiO_x matrix of the B/SiO_x powder, and large B particles (~1 μm) were present in the structure of the B/SiO_x powder. This was attributed to the MM power used to fabricate the B/SiO_x powder being insufficient, because B (Mohs hardness 9.5) is harder than Al (Mohs hardness 2.9) and Sn (Mohs hardness 1.8).

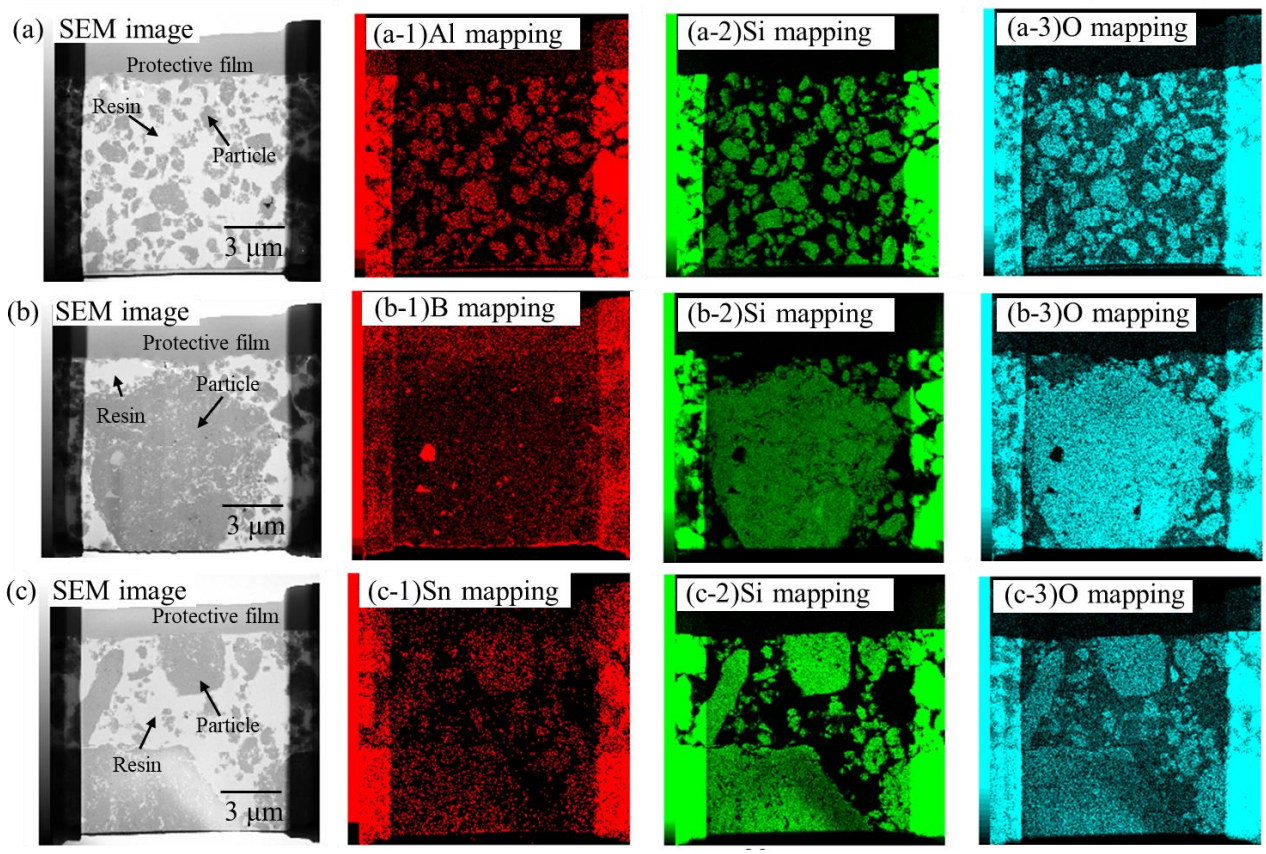

Figure 1-11. TEM images and EDS mappings of as-prepared (a) Al/SiO_x, (b) B/SiO_x, and (c) Sn/SiO_x particles.

Figure 1-12 shows the electrical resistivity values of pressed *M*/SiO_x (*M* = Al, B, and Sn) powders. The results confirmed that the addition of B or Sn increased the electronic conductivity of SiO_x by approximately one order of magnitude. Conversely, the electronic conductivity of the Al/SiO_x powder was comparable to that of SiO_x because the electrical resistivity of Al/SiO_x was comparable to that of SiO_x.

The Gibbs energies (Δ_rG^0) for the synthesis of Al_2O_3, B_2O_3, and SnO_2 are −594.61, 181.25, and 340.93 kJ mol^{-1}, respectively.

$$3SiO_2 + 4Al \rightarrow 3Si + 2Al_2O_3$$

$$3SiO_2 + 4B \rightarrow 3Si + 2B_2O_3$$

$$SiO_2 + Sn \rightarrow Si + SnO_2$$

The Δ_rG^0 values for the B/SiO_x and Sn/SiO_x powders were positive, indicating that SiO_2 was thermodynamically more stable than B_2O_3 and SnO_2. In contrast, the Δ_rG^0 value for the Al/SiO_x powder was negative, indicating that Al_2O_3 was thermodynamically more stable than SiO_2. Therefore, it was hypothesized that Al_2O_3, which is an insulator, formed because an oxidation reaction during sample preparation.

These results indicate that B and Sn[41] were dissolved in the SiO_2 matrices of B/SiO_x and Sn/SiO_x, respectively, during MM.

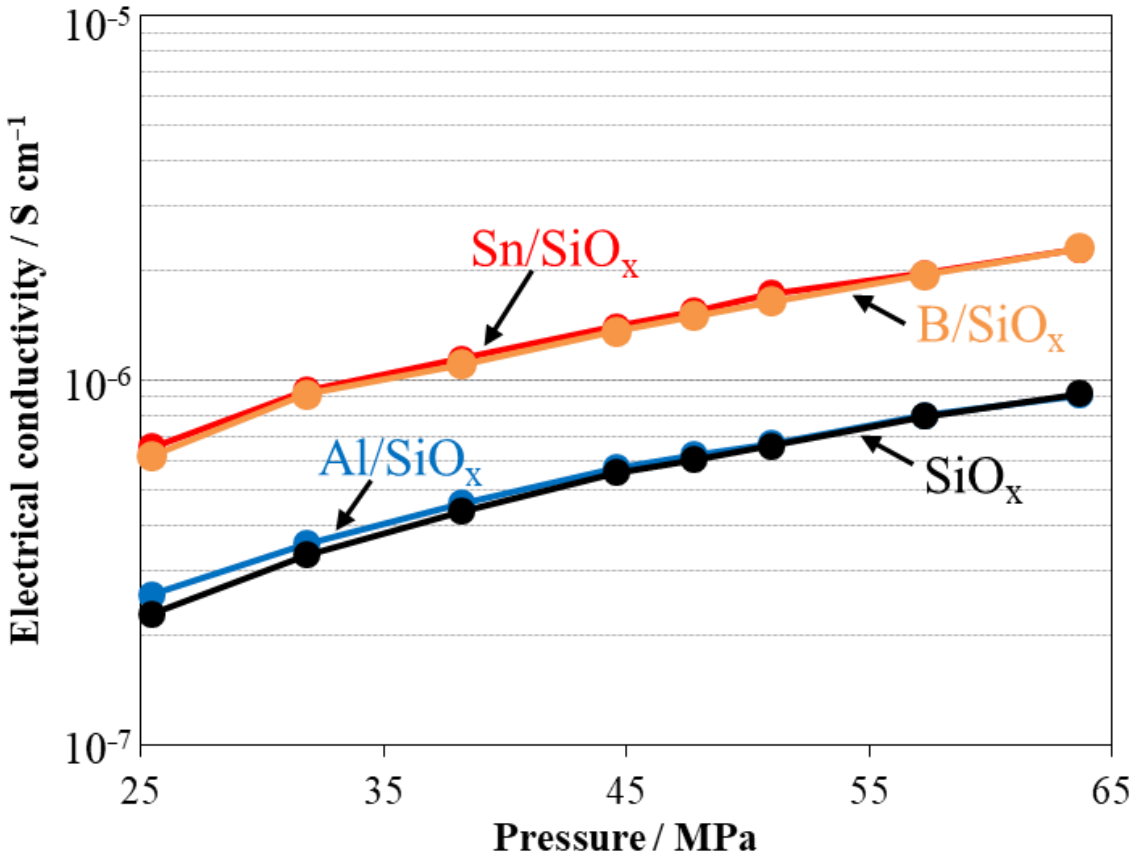

Figure 1-12. Electrical conductivities of the as-prepared SiO_x and M/SiO_x (M = Al, B, and Sn) powders under compression.

1.3.3 Charge–discharge properties

Figure 1-13 shows the dependence of the discharge capacity of M/SiO_x (M = Al, B, and Sn) electrodes on the cycle number in a 1 M LiTFSA solution in PC with a charge capacity limit of 1000 mA h g $(Si)^{-1}$ as the electrolyte. The performance of the SiO_x and Si electrodes was also evaluated for comparison. The capacity of the Si electrode decayed rapidly after 100 cycles, whereas the capacity of the SiO_x electrode started to decay only after 170 cycles. The cycle performance of the Al/SiO_x electrode was comparable to that of the

SiO_x electrode. However the cycle life of the B/SiO_x and Sn/SiO_x electrodes was longer (≥150 cycles). It was hypothesized that the addition of B and Sn to SiO_x improved the current-collecting properties of the electrodes because it increased the electron conductivity of SiO_x by approximately one order of magnitude.

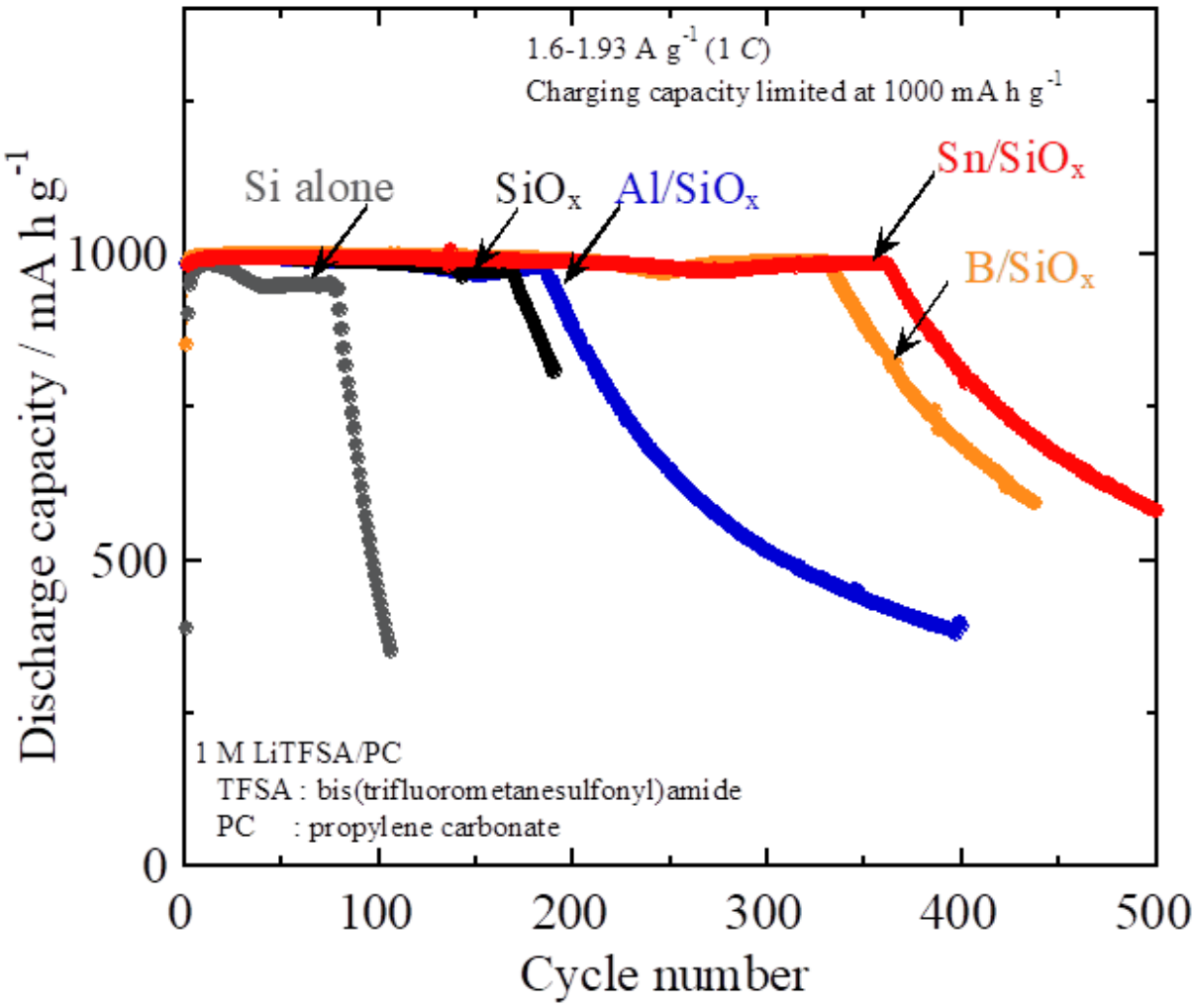

Figure 1-13. Dependence of the discharge capacity of Si and M/SiO_x (M = Al, B, and Sn) electrodes on the cycle number in a 1 M LiTFSA solution in PC with a charge capacity limit of 1000 mA h g $(Si)^{-1}$ as the electrolyte.

Figure 1-14 shows the charge–discharge curves of the SiO_x and M/SiO_x (M = Al, B, and Sn) electrodes in a 1 M LiTFSA solution in PC as the electrolyte after 1, 2, 100, 150, and 200 cycles. The decrease in discharge capacity was ascribed to the electrodes collapsing and conductive pathways becoming disconnected. Consequently, the discharge capacity decreased (Figure 1-13), current collection properties deteriorated, charge capacity decreased rapidly, and charge capacity did not reach 1000 mA h g^{-1} (Figure 1-14).

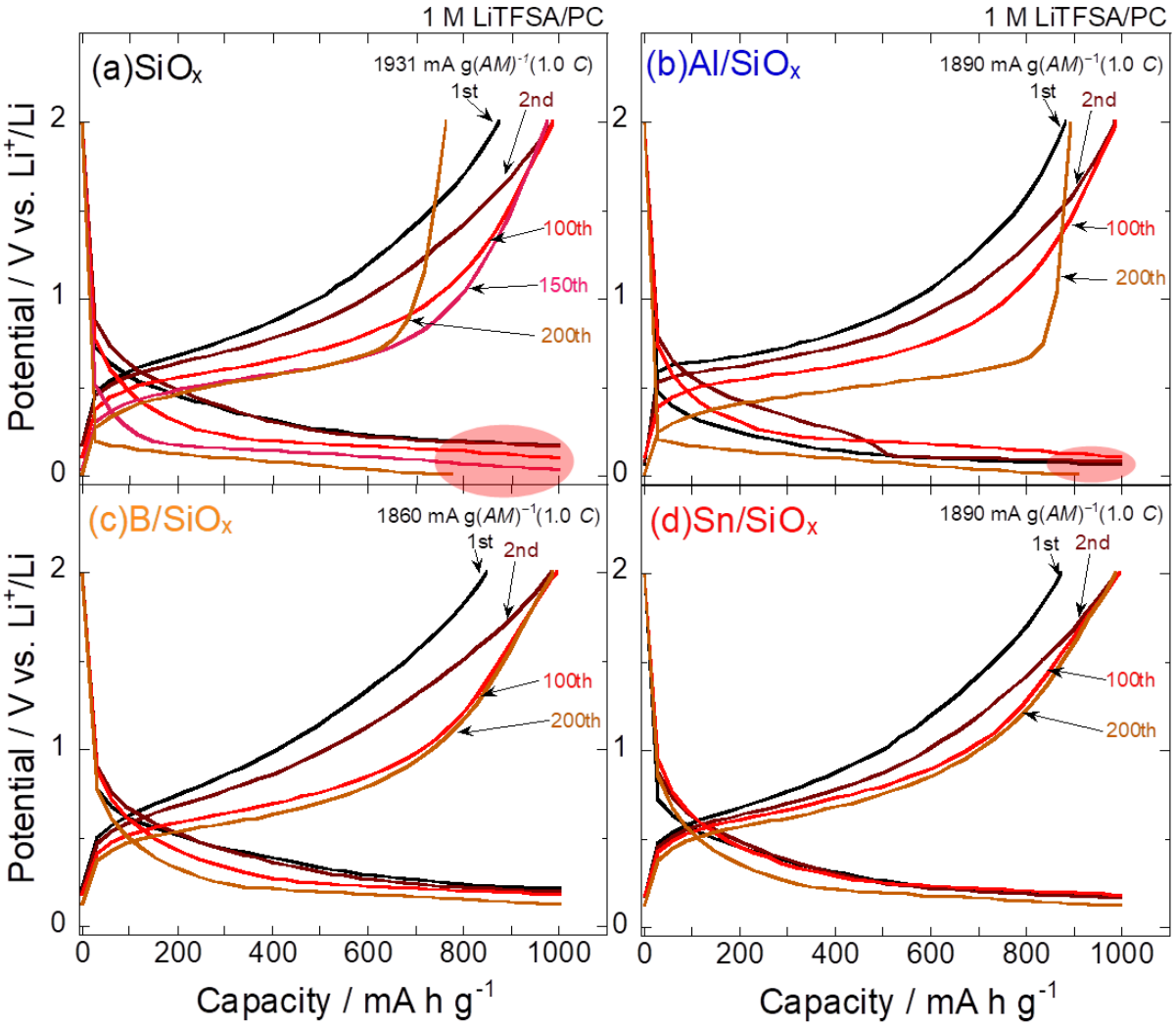

Figure 1-14. Charge–discharge curves of the SiO_x and M/SiO_x (M = Al, B, and Sn) electrodes in a 1 M LiTFSA solution in PC as the electrolyte after 1, 2, 100, 150, and 200 cycles.

To determine the reason for the aforementioned improvement in electrode properties, an active electrode material comprising only the SiO_x matrix was prepared, and its reaction was investigated. In addition, for the *M*/SiO_2 (*M* = Al, B, and Sn) samples, the changes in the reactivity of the electrode material with Li-ions after the addition of the third element were investigated. In other words, to determine the amount of occluded Li-ions, we conducted a test to determine the amount of Li-ions that reacted with the electrode material in the absence of capacity regulation. Figure 1-15(a) shows the dependence of the discharge capacities of the SiO_2 and *M*/SiO_2 (*M* = Al, B, and Sn) electrodes on the cycle number in a 1 M LiTFSA solution in PC as the electrolyte at 0.38 A g^{-1}. The temperature and potential range for testing were set to 303 K and 0.005−2.000 V vs. Li^+/Li, respectively. The capacities of the B/SiO_2 and Sn/SiO_2 electrodes were higher than that of SiO_2. First, the reaction of SiO_2 with Li-ions was slow, and SiO_2 did not present Li-ion storage properties. However, it has recently been reported that, amorphous SiO_2 reacts with Li-ions to form Si and lithium silicate ($Li_2Si_2O_5$), as follows:[42]

$$5SiO_2 + 4Li^+ + 4e^- \rightarrow 2Li_2Si_2O_5 + Si. \quad (1\text{-}1)$$

The XRD, TEM, and electron diffraction results (Figures 1-9 and 1-10) confirmed that SiO_2 was amorphous. In addition, the charge–discharge curves (Figures 1-15) and the differential capacity (dQ/dV) curves (Figures 1-16) after 10 cycles of the SiO_2 and *M*/SiO_2 (*M* = Al, B, and Sn) electrodes were obtained. The presence of the peaks of single-phase Si at ~0.5 V in

the discharge curves of the electrodes suggested that the reaction described by Equation (1-1) progressed. Therefore, in this study, we considered that the charge–discharge capacity of SiO_2, which became amorphous after MM, was not negligible. Furthermore, the capacities of the B/SiO_2 and Sn/SiO_2 electrodes were higher than that of the SiO_2 electrode, because the reactivity of the SiO_2 matrices with Li^+ ions was improved by the solid dissolution and uniform dispersion of B and Sn throughout the SiO_2 matrix (Figure 1-17(b)). Furthermore, it was considered that Al was oxidized and formed amorphous Al_2O_3, which was dispersed throughout the SiO_2 matrix because the electronic conductivity of Al/SiO_2 was comparable to that of SiO_2. Therefore, it was hypothesized that the capacity of the Al/SiO_2 electrode was comparable to that of the SiO_2 electrode because the reactivity of the electrode material with Li-ions was not improved by the addition of Al to SiO_2 and the reaction described by Equation (1-1) was not promoted.

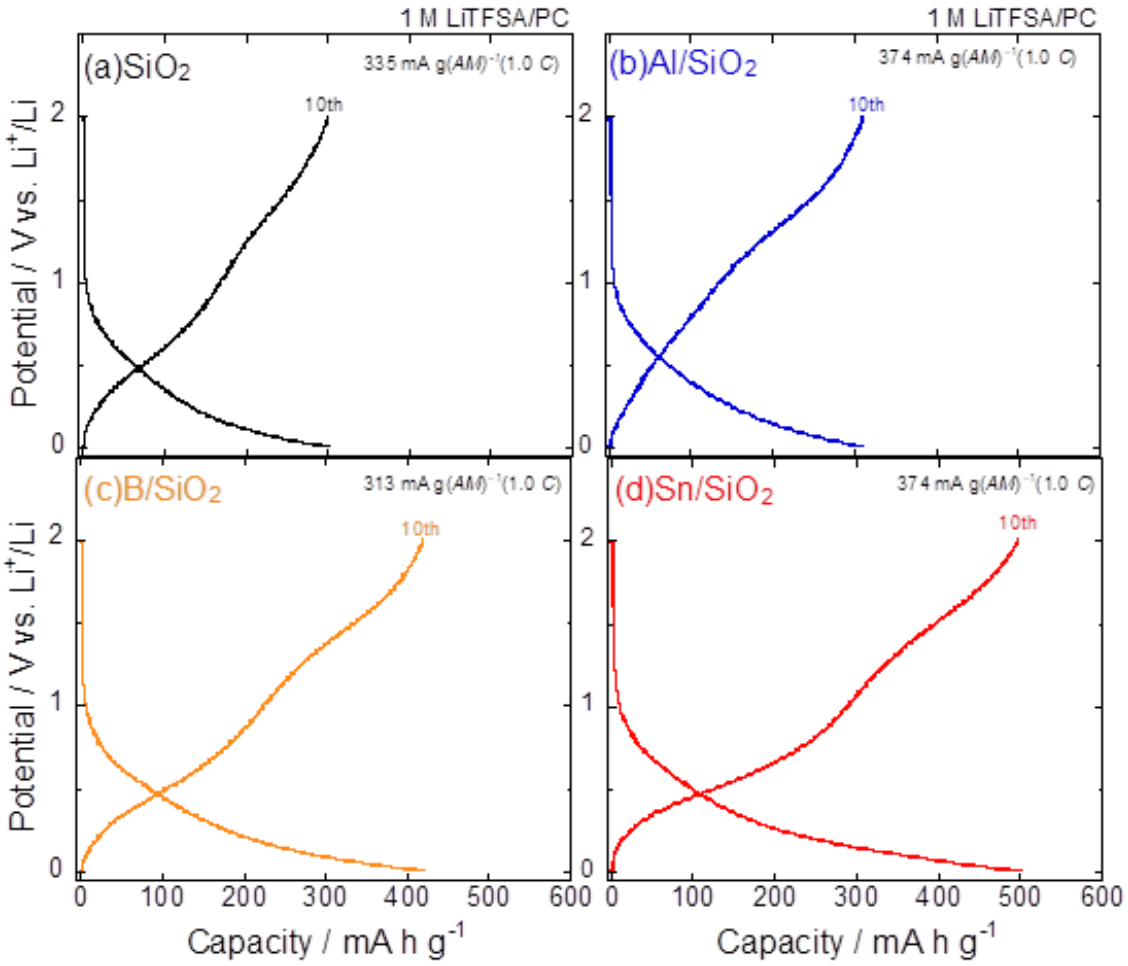

Figure 1-15. The charge–discharge curves of the SiO_2 and M/SiO_2 (M = Al, B, and Sn) electrodes in 1 M LiTFSA/PC after 10 cycles.

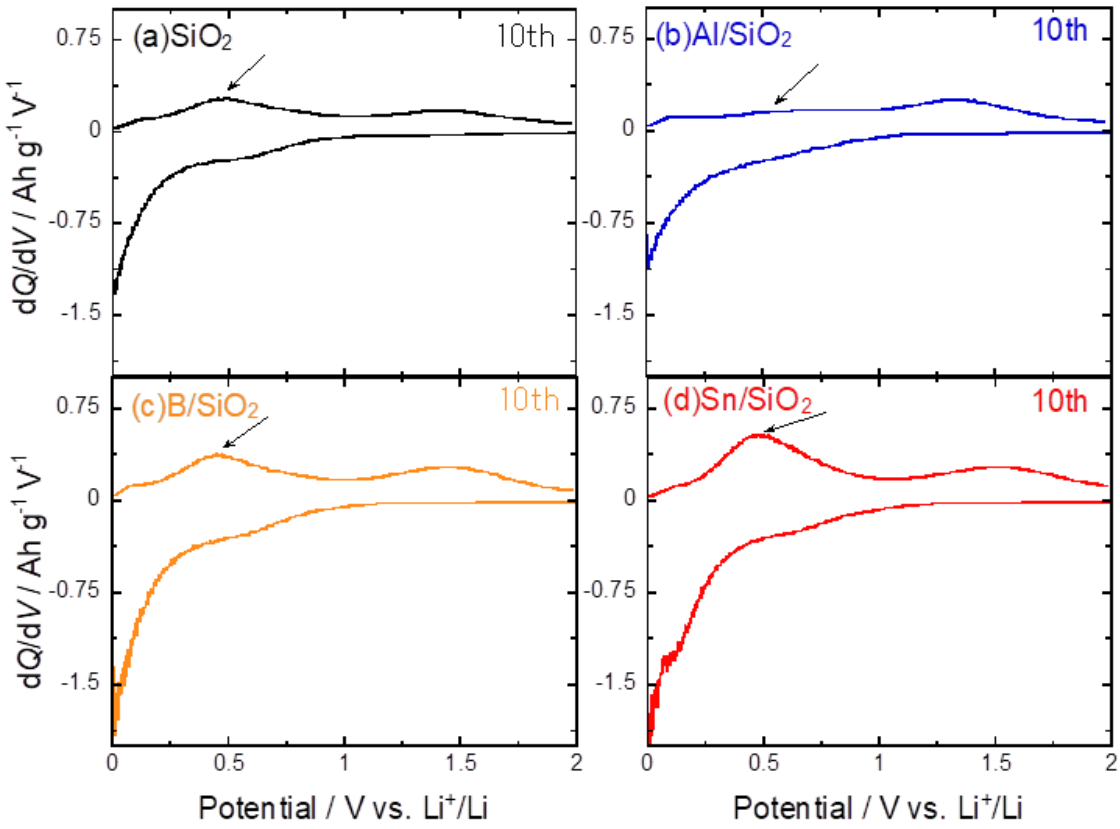

Figure 1-16. The dQ/dV plots on the charge-discharge side of the SiO_2 and *M*/SiO_2 (*M* = Al, B, and Sn) electrodes in 1 M LiTFSA/PC after 10 cycles.

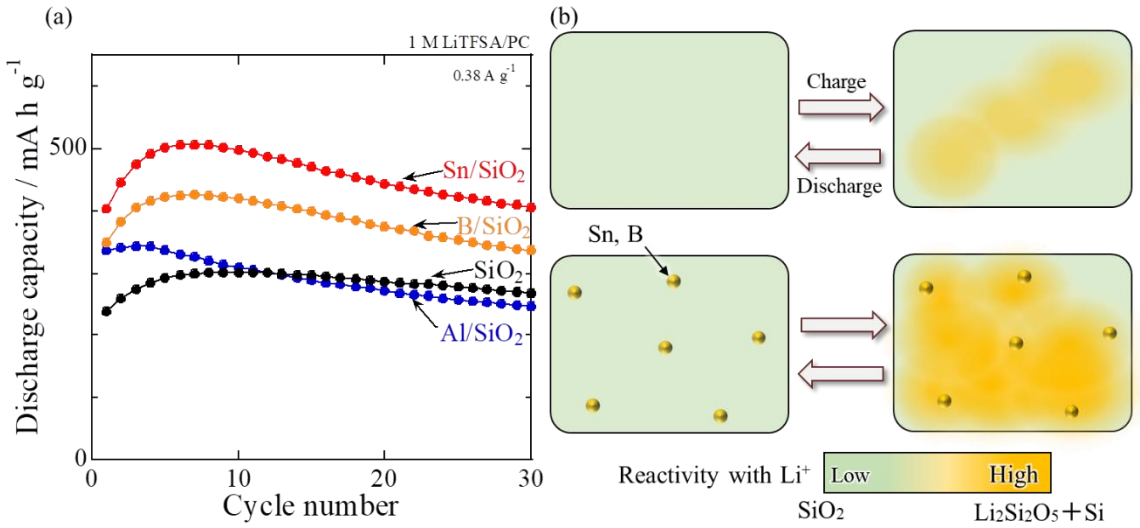

Figure 1-17. Dependence of the (a) discharge capacities of the SiO_2 and *M*/SiO_2 (*M* = Al, B, and Sn) electrodes on the cycle number in a 1 M LiTFSA solution in PC as the electrolyte at 0.38 A g^{-1}. The temperature and potential range for the test were set to 303 K and 0.005−2.000 V vs. Li^+/Li, respectively. (b) Schematics of the reactions of SiO_2 and *M*/SiO_2 (*M* = B, Sn) with Li-ions.

These results indicate that the cycle life of SiO_x was increased by adding B and Sn to SiO_x. Figure 1-18 shows a schematic of the improvement in the charge–discharge performance of the *M*/SiO_x (*M* = B, Sn) electrodes. Si participated in the following two-step Li alloying reactions during charging:[43–46]

$$a\text{-Si} + 2Li^+ + 2e^- \rightarrow a\text{-}Li_{2.00}Si, \quad (1\text{-}2)$$

$$a\text{-}Li_{2.00}Si + 1.75Li^+ + 1.75e^- \rightarrow c\text{-}Li_{3.75}Si, \quad (1\text{-}3)$$

where *a* and *c* denote amorphous and crystalline, respectively.

Once the reaction described by Equation (1-3) progressed, the electrode collapsed because the volume change caused by the formation of $Li_{3.75}Si$ (380 %) was larger than that caused by the formation of $Li_{2.00}Si$ (240 %).

For the experiments for which the charge capacity was limited to 1000 mA h g^{-1}, it was considered that Li alloying of Si occurred locally because the reactivities of the SiO_x and Al/SiO_x electrodes with Li-ions were poor. Consequently, $Li_{3.75}Si$, which presents a large volume change, was formed, and it was considered to have caused electrode collapse and capacity decline. Moreover, the electronic conductivities of the B/SiO_x and Sn/SiO_x electrodes, were higher than that of the SiO_x electrode, and the Li-ion reactivity of the SiO_2 matrices of the B/SiO_x and Sn/SiO_x electrodes was higher than that of the SiO_2 matrix of the SiO_x electrode. Therefore, the Si particles in the active material easily and uniformly reacted with Li-ions. Accordingly, the formation of $Li_{2.00}Si$ with a small volume change was suppressed. These results demonstrated that the cycle properties of the B/SiO_x and Sn/SiO_x electrodes were superior to those of the SiO_x electrode because the stress induced by to the volume expansion of Si could not accumulate during charging, the damage to the electrodes was negligible, and electrode disintegration was suppressed.

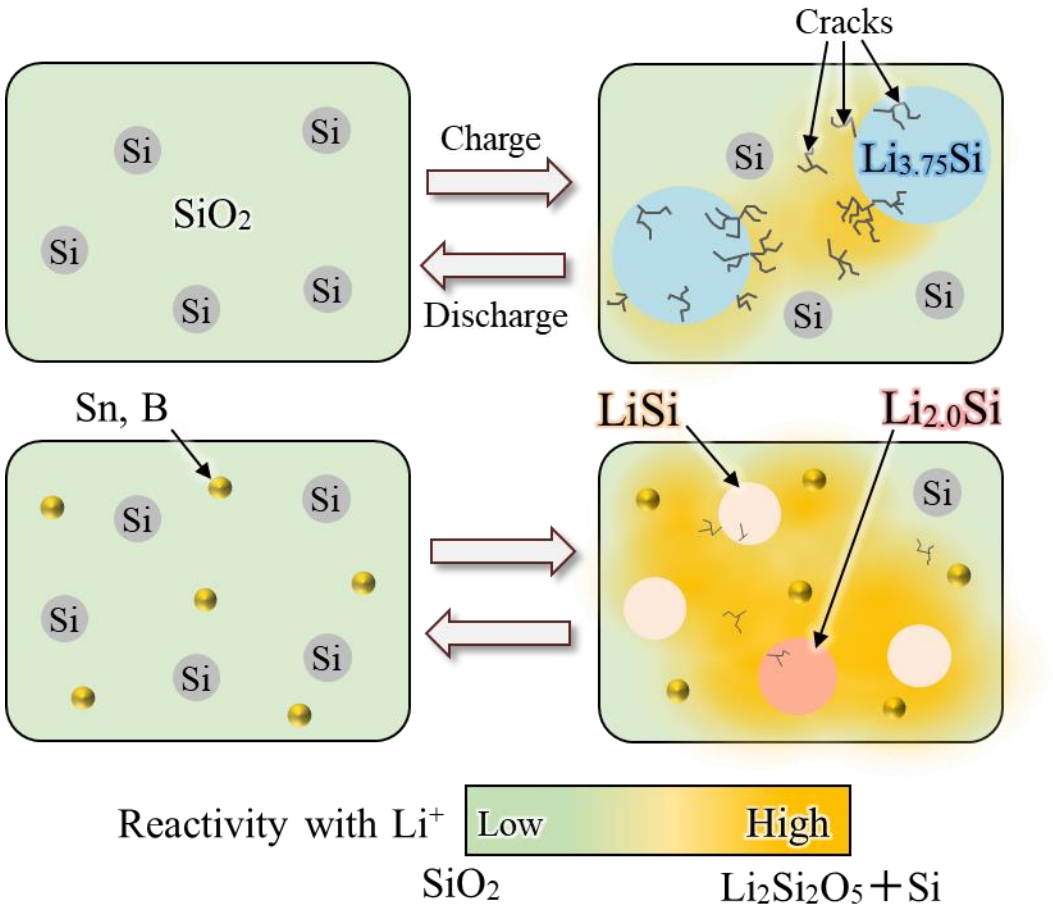

Figure 1-18. Schematic of the improvement in the charge–discharge performance of the *M*/SiO_x (*M* = B, Sn) electrodes.

These results indicate that the charge–discharge properties of the Sn/SiO_x and B/SiO_x electrodes were superior to those of the SiO_x electrode because the electronic conductivities of the Sn/SiO_x and B/SiO_x electrodes were higher than that of the SiO_x electrode. Figure 1-19 shows the rate properties of the SiO_x and *M*/SiO_x (*M* = Al, B, and Sn) electrodes. It was determined that the rate properties and cycle performance of the Sn/SiO_x and B/SiO_x electrodes were superior to those of the SiO_x electrode, as expected.

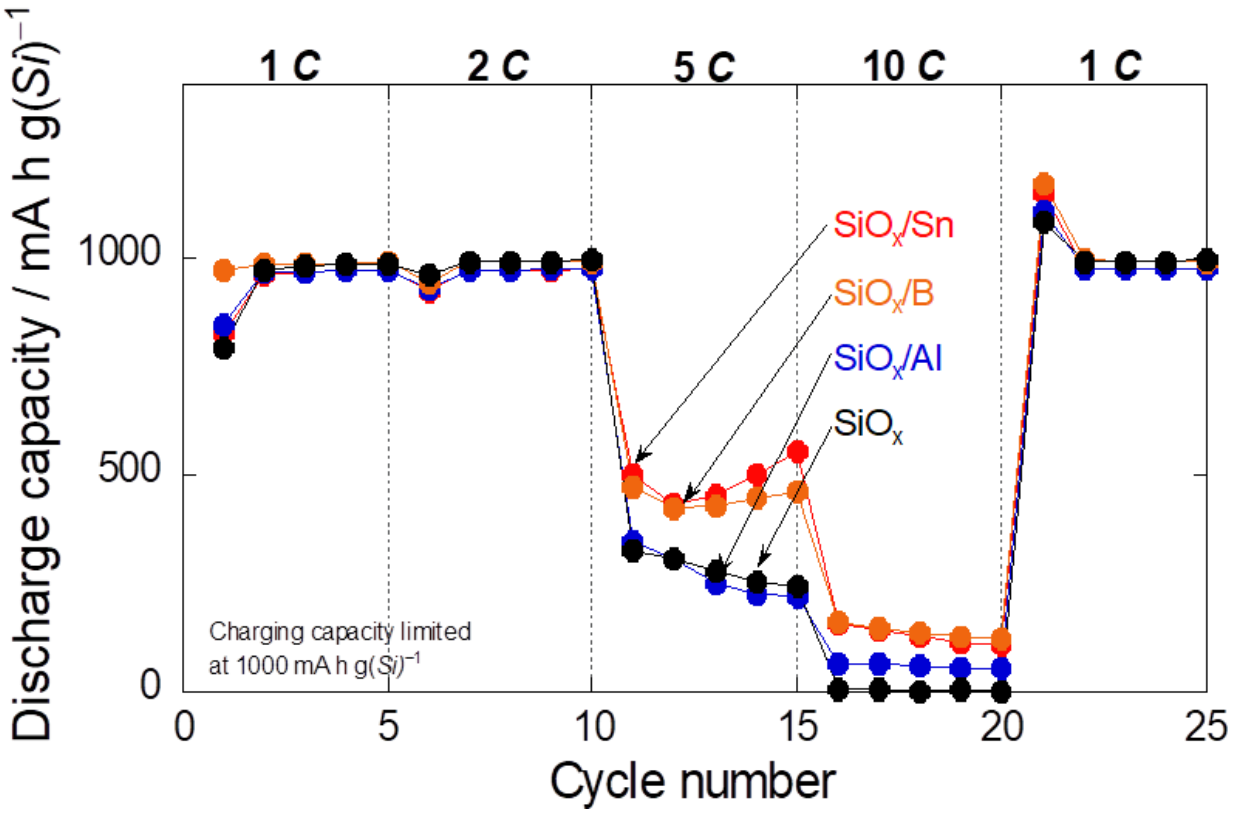

Figure 1-19. Changes in the discharge capacities of the SiO_x and M/SiO_x (M = Al, B, and Sn) electrodes with the cycle number in a 1 M LiTFSA solution in PC as the electrolyte with a charge capacity limit of 1000 mA h g $(Si)^{-1}$.

1.4 Summary

In this study, we prepared M/SiO_x (M = Al, B, and Sn) active materials by adding a third element to SiO_x using an MM method and investigated the properties of the M/SiO_x (M = Al, B, and Sn) active materials as anodes for Li-ion batteries. We confirmed that SiO_x comprised nanocrystalline Si dispersed throughout an amorphous-like SiO_2 matrix, and the third element was only present in the SiO_2 matrix. The electron conductivities of B/SiO_x and Sn/SiO_x were higher than that of SiO_x. However, the electron conductivity of Al/SiO_x was comparable to that of SiO_x. This was attributed to the formation of Al_2O_3, which is an insulator, via the oxidation of Al. The tests performed to evaluate the cycle properties of the

electrodes using a charge (Li-ion storage) capacity limit of 1000 mA h g^{-1} revealed that the cycle lives of B/SiO_x (330 cycles) and Sn/SiO_x (360 cycles) were longer than that of SiO_x (170 cycles). When SiO_2 becomes amorphous, the reaction of $5SiO_2 + 4Li^+ + 4e^- \rightarrow 2Li_2Si_2O_5 + Si$ (1-1) proceeds, and it is possible to form silicon and lithium silicate ($Li_2Si_2O_5$), which is a lithium-ion activity. The electronic conductivity was improved because they were present in the matrix and B and Sn were dispersed throughout the SiO_2 matrix. Therefore, this is because SiO_2 reacts uniformly with lithium ions due to the improvement of electronic conductivity so that the stress due to the volume change of Si is difficult to concentrate and the destruction of the electrode is reduced.

Chapter 2

Effect of Sn Addition on the Anode Properties of SiO_x for Lithium-Ion Batteries

2.1 Introduction

Li-ion batteries store renewable energy and can be used repeatedly without emitting CO_2; therefore, they can help achieve a low-carbon society. Furthermore, Li-ion batteries have attracted increasing attention as devices that can contribute to achieving a sustainable society because they do not contain Cd or Pb and present a small environmental load. Additionally, the electromotive force of Li-ion batteries is high (~4 V). Therefore, Li-ion batteries have recently been used for numerous applications, such as wearable devices, drones, and electric vehicles, and are expected to be used on aircrafts in the future.

Performant batteries present high energy densities. To improve the energy density of Li-ion batteries, the capacities of their cathode and anode materials should be high. For example, to increase the capacity of $LiCoO_2$ (~140 mA h g^{-1}) cathode material, compounds such as $LiNi_{0.8}Mn_{0.1}Co_{0.1}O_2$ (capacity of ~200 mA h g^{-1}), which is a layered oxide, have been used.[47,48] Moreover, researchers have developed Si-based anode materials because the theoretical capacity of Si (3600 mA h g^{-1}) is high (~10 times higher than that of graphite).[49] However, Si experiences large volume changes (~380 %) during alloying and dealloying with

Li-ions, and the stress generated during alloying–dealloying causes pulverization and electrical isolation of Si. This causes fatal structural failure and rapid capacity decrease.

Several researchers have examined this issue using various methods.[1–15] For example, upon coating Si with Ru, the mechanical properties of the anode material were improved and the anode presented excellent cycle properties because Ru relaxed the stress caused by the volume expansion and contraction of Si.[32] Additionally, Si and thermodynamically stable silicide were used to fabricate composites, and Ni was used to substitute Si and solid-dissolve in Si to improve the electrochemical performance of Si-based anode materials, including their Li-ion diffusivity, resulting in the excellent cycle properties and high-speed charge–discharge properties of the Si-based anode materials.[29]

Among various anode materials, SiO_x-based materials, such as those used for electric vehicles, have recently attracted increasing attention. We have previously demonstrated that SiO_x comprises a mixture of Si and SiO_2 phases, and nanosized clustered Si is finely dispersed throughout a SiO_4 tetrahedral matrix.[16] Therefore, the cycle properties of the SiO_2 matrix are superior to those of Si because the SiO_2 matrix relieves the stress induced by the volume expansion of Si during charging–discharging.[17]

However, the decrease in capacity of SiO_x with increasing number of charge–discharge cycles was considerably higher than that of graphite. This was attributed to the reaction of SiO_x with Li-ions becoming localized owing to the low electronic conductivity of SiO_x, and

that part becomes the starting point, cracks form, and lastly, the electrode disintegrates. Therefore, SiO_x and graphite mixtures are used as anode materials for the Li-ion batteries of electric vehicles. In the future, the SiO_x-to-graphite mixing ratio should be increase to extend battery life and further increase the driving range of electric vehicles. Therefore, it is critical to improve the properties of SiO_x-based anode materials.

Numerous studies have been conducted on SiO_x-based anode materials.[18–21] For example, the anode materials fabricated by adding porous Si to SiO_x[23] or developing core–shell Si–SiO_x nanocomposites,[24,25] presented ample space for the volume expansion and contraction of Si during charge–discharge. In addition, the electrical conductivity of SiO_x-based anode materials was improved by mixing SiO_x with carbon.[26] However, to the best of our knowledge, no studies have focused on the SiO_2 matrix and improving its properties.

The method developed herein is noteworthy. Conventional SiO_x is manufactured by mixing Si and SiO_2, heating and then cooling the mixture, precipitating the generated SiO gas, and precipitating fine Si particles via a disproportionation reaction ($2SiO \rightarrow Si + SiO_2$).[28] However, controlling the Si-to-SiO ratio is challenging because the boiling point of SiO (2153 K) is considerably lower than that of Si (3538 K). Therefore, we used an MM method because it allowed us to design various materials regardless of the melting points of the raw materials.

We have recently developed a new method for improving the properties of SiO_x-based anode materials by increasing the electronic conductivity of the SiO_2 matrix. *M*/SiO_x (*M* = Al, B, and Sn) anodes for Li-ion batteries were manufactured using an MM method, which allowed the fabrication of various materials and did not involve the conventional SiO gas-phase state. The charge–discharge properties of the *M*/SiO_x (*M* = Al, B, and Sn) anode materials were evaluated, and the effect of the addition of the third element (*M*) on the anode properties was investigated.[50] In particular, the cycle life of the Sn/SiO_x anode material was longer than that of SiO_x. Upon dispersing Sn throughout the SiO_2 matrix, the electronic conductivity of the anode material increased, and SiO_2 uniformly occluded and released Li-ions (Figure 2-1). The structure prevented the stress induced by the volume change of Si from concentrating, thereby hindering electrode disintegration.[50]

In this study, we investigated the effect of the amount of Sn added to SiO_x on the properties of Sn/SiO_x anode materials and in particular on their cycle life.

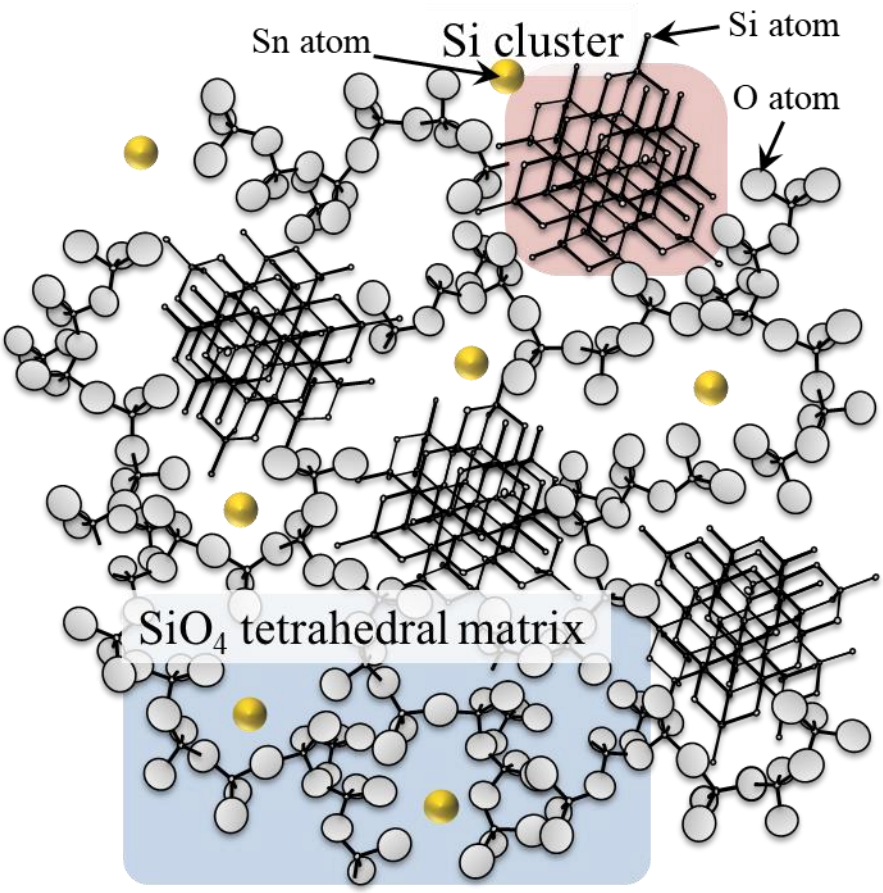

Figure 2-1. Schematic of the as-fabricated Sn/SiO_x anode material.

2.2 Experimental

2.2.1 Sample preparation

2.2.1.1 Preparation of SiO_x and y wt.% Sn/SiO_x (y = 1, 3) powders

Si powder was prepared using a mass-produced gas atomizer according to a previously described procedure.[50]

To prepare SiO_x powder, gas-atomized Si powder (32.4 g) and commercially available

SiO_2 powder (27.6 g; purity 99.9 %; Kojundo Chemical Lab. Co. Ltd.) were mixed at a mass ratio of 54:46. The mixed powder was added to an austenite stainless-steel vessel filled with crushed high-carbon chromium-bearing steel (C 1 wt.%, Cr 1 wt.%) balls (Φ19 mm) with the total mass of 12 kg. The active-material–to–balls mass ratio was 1:200.

Y wt.% Sn/SiO_x (y = 1, 3, and 5 wt.%) powders were prepared according to the same process used to fabricate SiO_x powder, except for the amounts of raw material powders. The 1 wt.% Sn/SiO_x powder was fabricated using 32.1 g of Si powder, 27.3 g of SiO_2 powder, and 0.6 g of Sn powder, whereas the 3 wt.% Sn/SiO_x powder was manufactured using 31.4 g of Si powder, 26.8 g of SiO_2 powder, and 1.8 g of Sn powder. The 5 wt.% Sn/SiO_x powder was manufactured using 30.8 g of Si powder, 26.2 g of SiO_2 powder, and 3.0 g of Sn powder.

The austenite stainless-steel vessels were sealed, evacuated to a pressure of 0.1 MPa, and then dry Ar gas was used to fill by gas replacement. The vessels were attached to a vibrating ball mill (MB-1, Chuo Kakohki Co.), and the powder mixtures were subjected to MM for 14 h at an amplitude of ± 4 mm and frequency of 1200 rpm. Thereafter, the number of balls was increased to achieve an active-material–to–crushed balls mass ratio of 1:300, and MM was continued for 14 h.

The particle size of the as-obtained powders was adjusted to ≤ 10 μm using a jet mill (Co-Jet, Seishin Enterprise Co., Ltd.), which crushed the agglomerated powder via collision

between powder particles under a N_2 gas stream with a pressure of 0.7 MPa. This step was performed to obtain the target samples (Figure 2-2). The shapes of the powders were confirmed using SEM (Figure 2-3).

Figure 2-2. Photographs of a mixture of Si, SiO_2, and Sn powders before MM and 3 wt.% Sn/SiO_x powder obtained via MM.

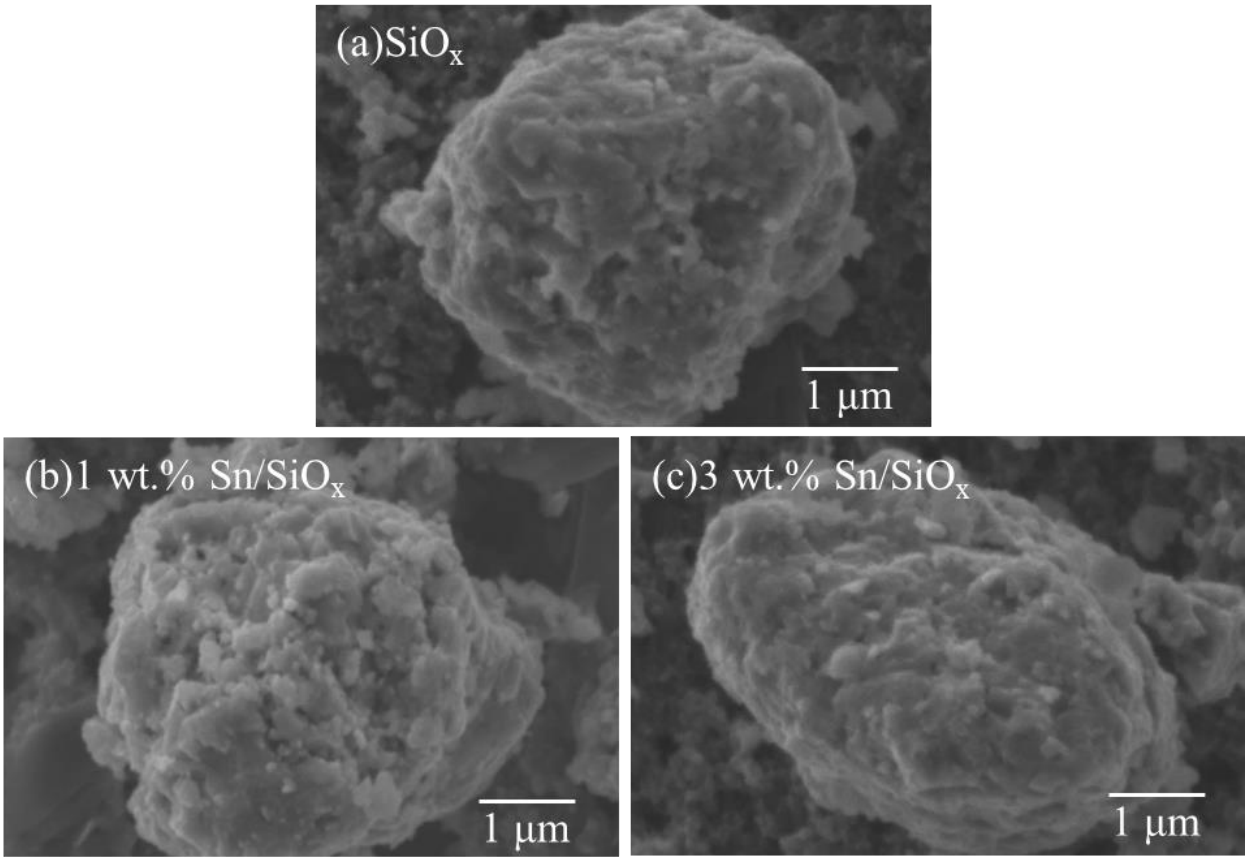

Figure 2-3. SEM images of as-prepared (a) SiO_x, (b) 1 wt.% Sn/SiO_x, and (c) 3 wt.% Sn/SiO_x

2.2.1.2 Preparation of Sn/SiO_2 and SiO_2 powders

For comparison, SiO_2 and Sn/SiO_2 powders were fabricated using the same process by subjecting SiO_2 and a mixture of SiO_2 and Sn to MM. This allowed us to analyze the changes in the properties of the SiO_2 matrix (reactivity with Li-ions) caused by the presence of Sn.

Commercially available SiO_2 powder was weighed and placed in a zirconia vessel filled with Φ5 mm zirconia crushed balls. Moreover, mixtures of commercially available

SiO_2 and Sn powders (purity 99.9 %, 325 mesh, Rare Metallic Co.) with mass ratios of 98:2 and 94:6 were used to fabricate 1 wt.% Sn/SiO_2 and 3 wt.% Sn/SiO_2, respectively. The powder mixtures (1.5 g) were placed in zirconia vessels filled with 100 g of Φ5 mm zirconia crushed balls. The vessels were sealed and placed in a PL-7 premium line planetary ball mill. The powder mixtures were subjected to MM at 380 rpm to prepare the target powders.

2.2.2 Analysis of the as-obtained samples

The Si crystallite sizes of the as-prepared SiO_x and y wt.% Sn/SiO_x (y = 1, 3) powders were measured using an XRD (RINT-2500, Rigaku) instrument with Cu Kα radiation operated at 50 kV and 200 mA, at a scanning rate of 4° m^{-1}, and in the scanning range of 20–70°.

The morphologies of the powders were observed using a SEM (JSM-6490LV, JEOL Ltd.) device operated at 5 kV. The measurement methods and conditions have been previously described.[50]

The size and dispersibility of nanocrystalline Si and Sn were observed using a TEM (JEM-F200, JEOL Ltd.) apparatus operated at 200 kV. To prepare the samples for TEM analysis, the as-prepared powders were embedded in a conductive thermosetting resin.

Subsequently, a carbon protective film was deposited on the surface of each sample, and then the samples were cut into ~10 μm × 10 μm × 100 nm specimens using a high-performance focused ion beam device (MI4050, Mo mesh, Hitachi High-Tech Corp.). We used a method to decrease the beam diameter to obtain information in the measurement range of ~1.2–1.3 nm and confirm the presence of nanocrystalline Si using electron diffraction and EDS data.

The electronic conductivity of the as-prepared powders was evaluated using a powder resistivity measuring unit (MCP-PD51, Mitsubishi Chemical Analytech Co., Ltd.) with four probes. Samples of the as-obtained powders (~3 g) were placed in a Φ10 mm sample holder and compressed to a maximum pressure of 64 MPa to measure their volumetric electronic conductivity (Figure 2-4).

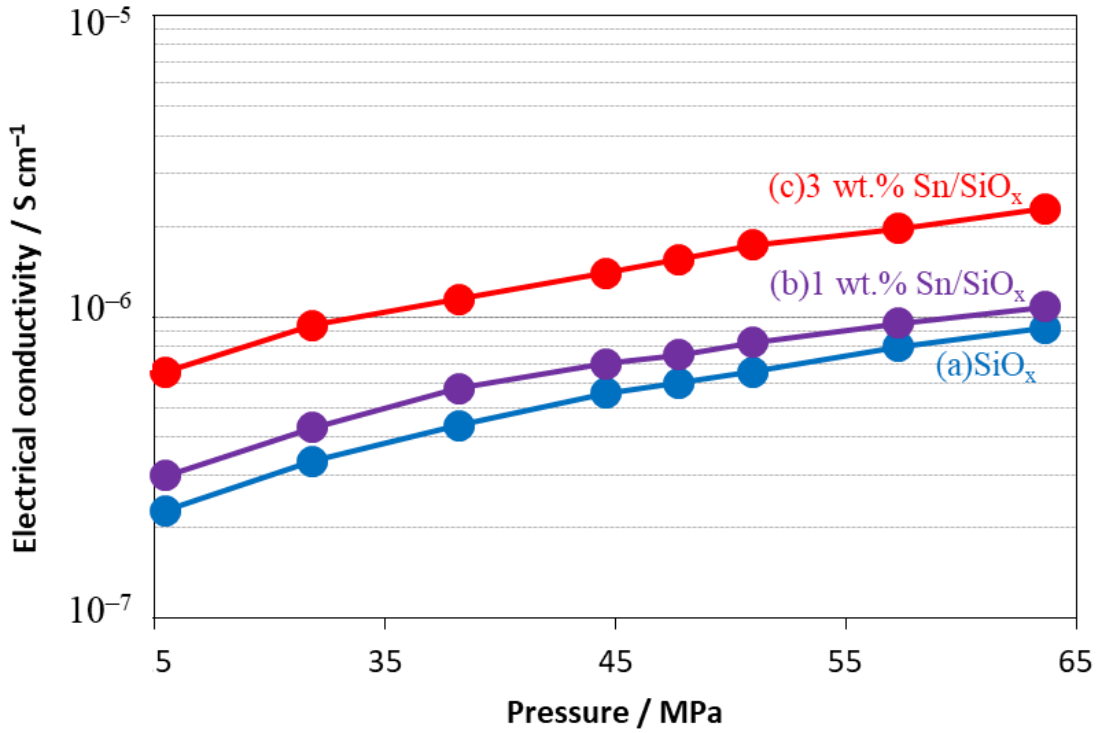

Figure 2-4. Electronic conductivity of the as-fabricated SiO_x, 1 wt.% Sn/SiO_x, and 3 wt.% Sn/SiO_x powders subjected to compression.

2.2.3 Electrode preparation

SiO_x, 1 wt.% Sn/SiO_x, 3 wt.% Sn/SiO_x, SiO_2, 1 wt.% Sn/SiO_2, and 3 wt.% Sn/SiO_2 powders were mixed with acetylene black, carboxymethyl cellulose, and styrene–butadiene rubber at a mass ratio of 70:15:10:5 using a kneading machine. Afterward, each mixture was coated on a Cu foil (coating mass per unit of surface area ~1.0 mg cm^{-2}) to fabricate mixed electrodes.

2.2.4 Cell assembly and charge–discharge tests

For the charge–discharge tests, 2032-type coin cells were assembled using each of the aforementioned electrodes as the working electrode, a Li metal sheet as the counter electrode, and a glass fiber filter as the separator. A 1 M solution of LiTFSA in PC was used as the electrolyte.

The SiO_x, 1 wt.% Sn/SiO_x, and 3 wt.% Sn/SiO_x electrodes were subjected to galvanostatic charge–discharge cycling tests using an electrochemical measurement system in the potential range of 0.005–2.000 V vs. Li^+/Li. The current density and measurement temperature were set to 1.90–1.93 A g^{-1} (1.0 *C*) and 303 K, respectively. Electrochemical measurements were performed using charge limits of 1000 and 750 mA h g^{-1}. In this study, a mixture of Si and SiO_2 was used, and SiO_2 was inactive toward Li-ions. The theoretical capacity of each electrode was calculated assuming that only Si reacted with Li-ions. The maximum alloying composition was calculated to be $Li_{15}Si_4$. The theoretical capacities of the SiO_x, 1 wt.% Sn/SiO_x, and 3 wt.% Sn/SiO_x electrodes were calculated to be 1931, 1922, and 1903 mA h g^{-1}, respectively.

For the SiO_2, 1 wt.% Sn/SiO_x, and 3 wt.% Sn/SiO_x electrodes, galvanostatic charge–discharge tests were performed in the potential range of 0.005–2.000 V vs. Li^+/Li, at a current density of 0.38 A g^{-1}, and at a temperature of 303 K.

2.3 Results and Discussion

Because the target powders were prepared using MM, the Sn and the raw material powders can react with each other or Sn can dissolve in Si because of the high energy generated during the collisions of the zirconia balls with each other or the powders. Therefore, first, we determined whether clusters of Si were dispersed throughout the SiO_2 matrix, in which Sn was dispersed as intended (Figure 2-1).

Figure 2-5 (a) shows the XRD patterns of the as-prepared SiO_x, 1 wt.% Sn/SiO_x, and 3 wt.% Sn/SiO_x powders in the 2θ range of 20–70°. The characteristic peaks of Si at (111), (220), and (311) were present in the XRD patterns of all powders. The size of the Si crystallites was calculated to be ~8–12 nm using the Scherrer's formula. The characteristic peak of SiO_2 was not observed in the XRD patterns of the powders. This was attributed to SiO_2 becoming amorphous-like owing to the high-energy pulverization during MM.

The characteristic peaks of elemental Sn and its compounds were not observed in the XRD patterns of the powders. Typically, the characteristic peak of Si up- or downshifts upon dissolving Sn in Si, because the crystal lattice of Si expands or contracts, respectively.[40] For example, the Si (111) peak upshifted by 0.06° upon the addition of 0.1 wt.% of Sn to it.[40] However, the diffraction peaks of Si did not shift (Figure 2-5 (b)) even though the amount of Sn in this study was 10–30 times higher than that. These results confirmed that Sn did not

dissolve in Si.

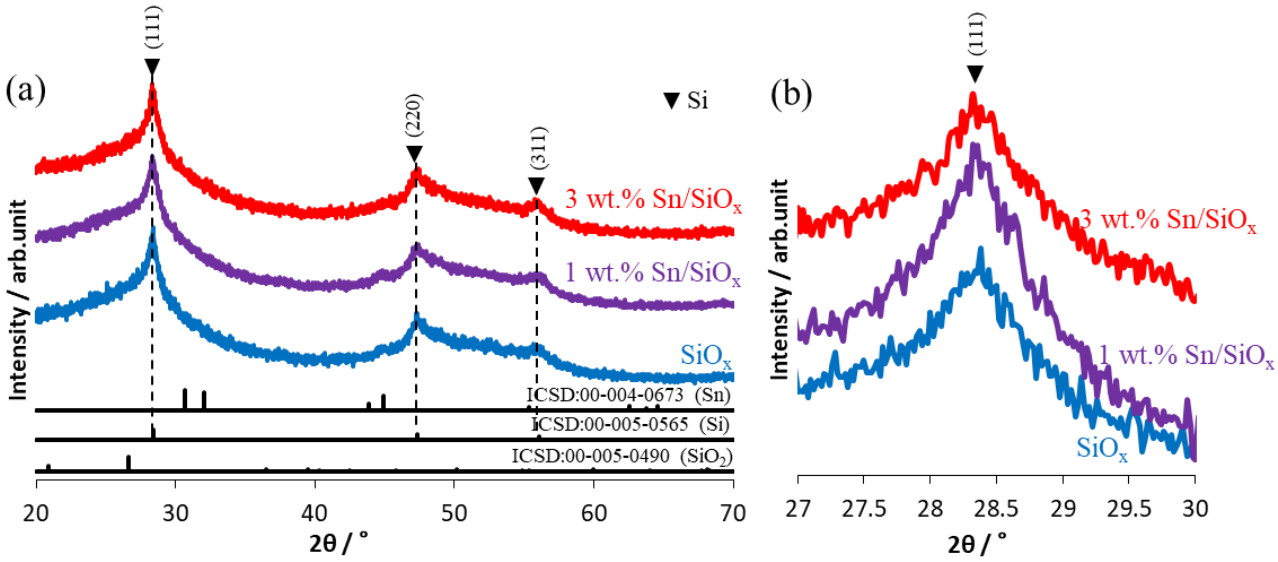

Figure 2-5. XRD patterns of the as-prepared SiO_x, 1 wt.% Sn/SiO_x, and 3 wt.% Sn/SiO_x powders in the 2θ ranges of (a) 20–70° and (b) 27–30°.

The detailed structure of the as-prepared powders was analyzed using TEM. Figure 2-6 shows the bright-field TEM images of SiO_x, 1 wt.% Sn/SiO_x, and 3 wt.% Sn/SiO_x particles and the EDS analysis values. The electron diffraction and EDS measurement range was 1.2–1.3 nm.

The areas encircled with light-blue dashed lines (i.e., areas (1), (2), and (3)) in the TEM images of the powders were confirmed to be Si using the electron diffraction data. Furthermore, the size of the Si nanocrystals was determined to be ~10 nm. Moreover, the electron diffraction patterns revealed that most of the regions outside areas (1), (2), and (3) comprised nanocrystals or amorphous phases. Therefore, the regions outside areas (1), (2),

and (3) were considered to comprise amorphous Si oxides because the EDS data revealed that they comprised 78.0 wt.% Si and 22.0 wt.% O for the SiO_x powder; 69.9 wt.% Si, 29.0 wt.% O, and 1.1 wt.% Sn for the 1 wt.% Sn/SiO_x powder; and 73.8 wt.% Si, 24.0 wt.% O, and 2.2 wt.% Sn for the 3 wt.% Sn/SiO_x powder.

The TEM and XRD data indicated that Sn was uniformly dispersed throughout the SiO_2 matrices of 1 wt.% Sn/SiO_x and 3 wt.% Sn/SiO_x.

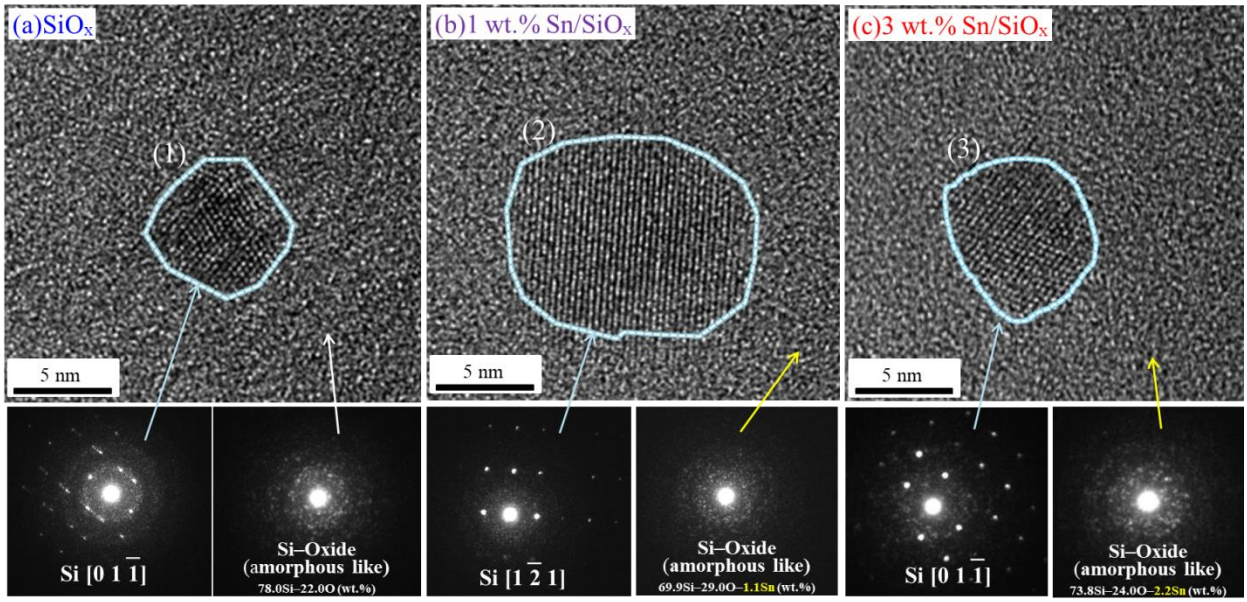

Figure 2-6. TEM images of as-prepared (a) SiO_x, (b) 1 wt.% Sn/SiO_x, and (c) 3 wt.% Sn/SiO_x powders.

Figure 2-7 shows the dependence of the discharge capacity of the SiO_x, 1 wt.% Sn/SiO_x, and 3 wt.% Sn/SiO_x electrodes on the cycle number in a 1 M LiTFSA solution in PC as the electrolyte with charge capacity limits of 1000 and 750 mA h g$(Si)^{-1}$. For comparison, SiO_x

and Si electrodes were also evaluated. The initial coulombic efficiencies of SiO_x, 1 wt.% Sn/SiO_x, 3 wt.% Sn/SiO_x, and 5 wt.% Sn/SiO_x were 87.3 %, 86.8 %, 84.2 %, and 85.7 %, respectively. However, because no relationship can be established between the amount of Sn added and initial coulombic efficiency, we only evaluated the cycle properties of the electrodes in this study.

The capacity of the Si electrode faded rapidly over 100 cycles. Conversely, the decrease in capacity of the SiO_x electrode was suppressed for 170 cycles. Furthermore, the discharge capacities of the 1 wt.% Sn/SiO_x and 3 wt.% Sn/SiO_x electrodes were maintained for 250 and 360 cycles, respectively, and the charge–discharge cycle life of the y wt.% Sn/SiO_x (y = 1, 3, and 5) electrodes increased with increasing Sn loading amount. This was attributed to the addition of Sn improving the electronic conductivity of SiO_x, which improved the current-collecting properties of the electrodes. However, the capacity of the 5 wt.% Sn/SiO_x electrode was maintained for 260 cycles; therefore, the performance of the 5 wt.% Sn/SiO_x electrode was comparable to that of the 1 wt.% Sn/SiO_x electrode (Figure 2-8). This was attributed to the electronic conductivity of SiO_x increasing upon adding 5 wt.% Sn to it, which improved current-collecting properties of the electrode. The electronic conductivities of the SiO_x and 5 wt.% Sn/SiO_x powders subjected to a pressure of 64 MPa were 9.2×10^{-7} and 36×10^{-7} S cm^{-1}, respectively.

The primary goal of this study was to confirm the effect of the addition of Sn on the

charge–discharge properties of SiO_x. For the experiment performed under a regulated charge capacity > 1000 mA h g^{-1}, the utilization rate of Si was high, such that the effect of the volume change of Si was considerable and the changes in cycle properties were small. Accordingly, it was challenging to elucidate the effect of Sn addition to the SiO_2 matrix. Therefore, to determine the effect of Sn addition to the SiO_2 matrix, we used a charge capacity of 750 mA h g^{-1} and a low Si utilization rate. In addition, the charge capacity was set to 750 mA h g^{-1}, which was more than twice as high as that of graphite.

Furthermore, the test was conducted by decreasing the Li insertion amount from 1000 to 750 mA h g^{-1} to observe the effect of Sn addition on the on the charge–discharge properties of SiO_x. The results are shown in Figure 2-7. For a Li insertion amount of 750 mA h g^{-1}, the difference between the cycle life of the SiO_x and 1, 3, or 5 wt.% Sn/SiO_x electrodes was larger than that observed at 1000 mA h g^{-1} (Figure 2-8). Furthermore, the discharge capacity of the 3 wt.% Sn/SiO_x electrode was maintained for 540 cycles. This was attributed to the volume change of Si decreasing, and electrode disintegration owing to stress being hindered by decreasing the amount of Li inserted. Therefore, it was concluded that the effect of Sn addition on the cycle properties of the SiO_2 matrix was significant, and cycle life can be extended by adjusting the amount of added Sn.

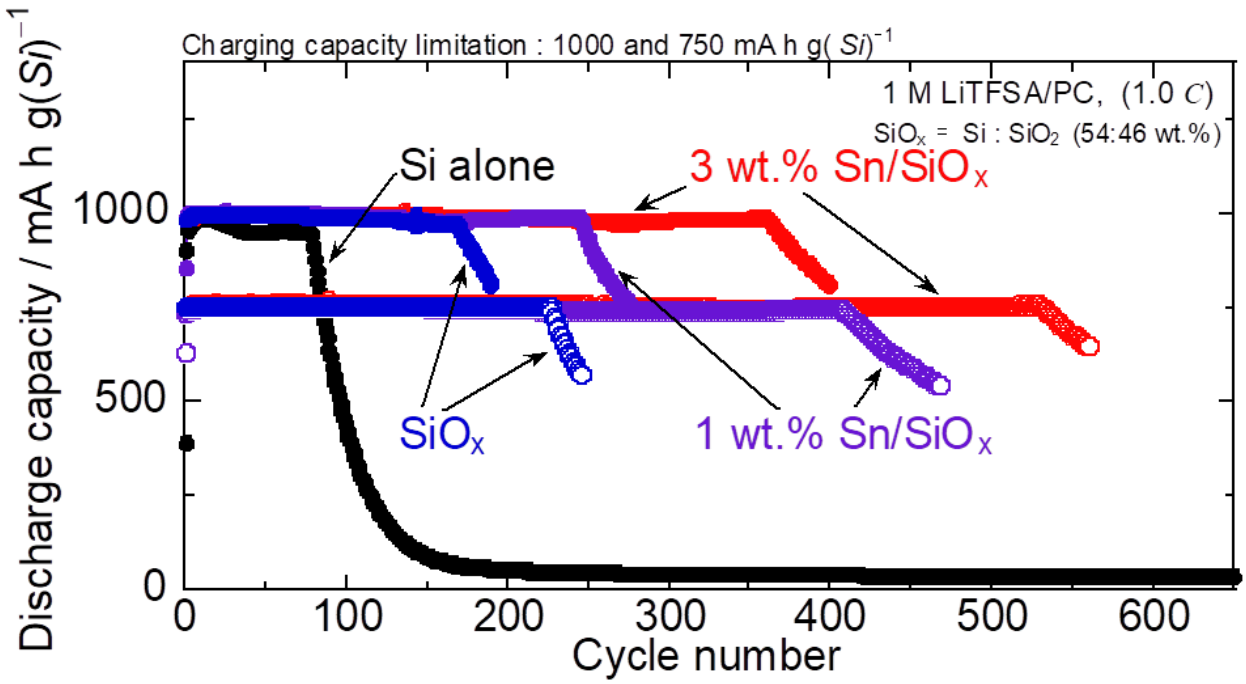

Figure 2-7. Dependence of the discharge capacities of the Si, SiO_x, 1 wt.% Sn/SiO_x, and 3 wt.% Sn/SiO_x electrodes on the cycle number A 1 M LiTFSA solution in PC with charge capacity limits of 1000 and 750 mA h g$(Si)^{-1}$ was used as the electrolyte

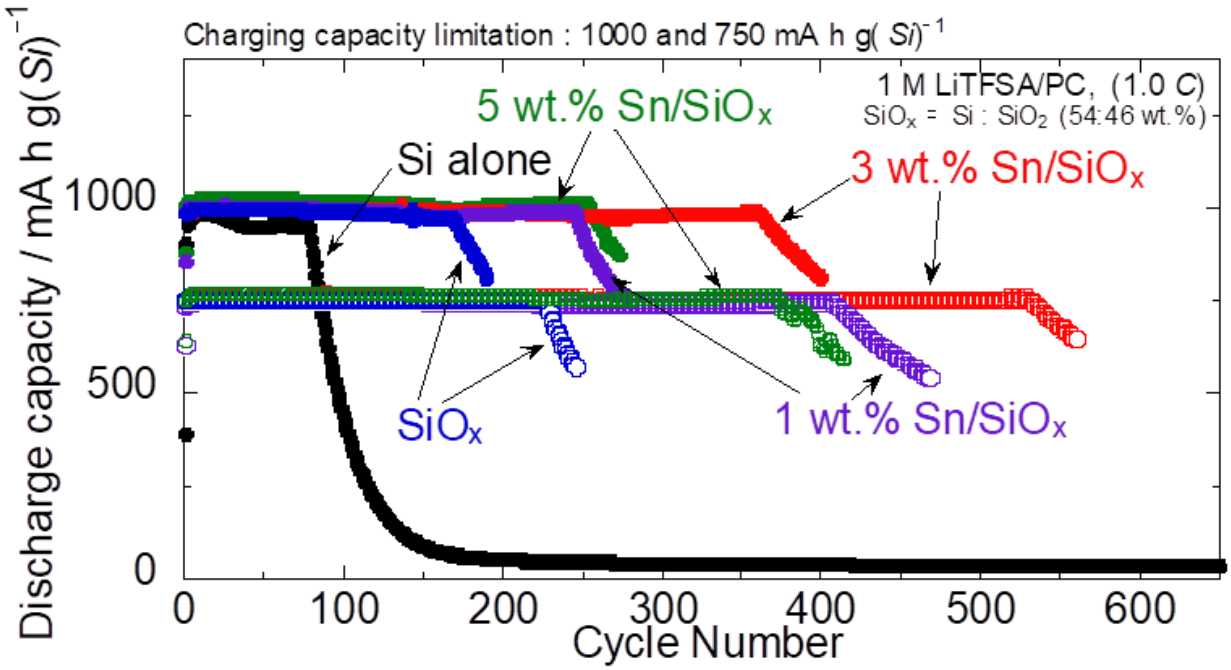

Figure 2-8. Dependence of the discharge capacities of the Si, SiO_x, 1 wt.% Sn/SiO_x, 3 wt.% Sn/SiO_x, and 5 wt.% Sn/SiO_x electrodes on the cycle number in a 1 M LiTFSA solution in PC with charge capacity limits of 1000 and 750 mA h g$(Si)^{-1}$ as the electrolyte.

The y wt.% Sn/SiO_x electrodes comprised Si and SiO_2 matrices in which Sn was uniformly dispersed. To determine the reason for the aforementioned improvement in electrode properties, we focused on the SiO_2 matrix. To investigate the effect of the properties of the SiO_2 matrix on the cycle life, a Sn/SiO_2 electrode was prepared and subjected to charge–discharge tests.

Figure 2-9 (a) shows the charge–discharge cycle test results of 1 wt.% Sn/SiO_2 and 3 wt.% Sn/SiO_2 electrodes. For comparison, the test results of a SiO_2 electrode are also presented. Typically, crystalline SiO_2 does not react with Li-ions and does not present a

charge–discharge capacity. However, in this study SiO_2 reacted with Li-ions to form amorphous SiO_2. It has been reported that amorphous SiO_2 can react with Li-ions to form Si and $Li_2Si_2O_5$, which is a Li-ion activity, according to the reaction described by the following equation:

$$5SiO_2 + 4Li^+ + 4e^- \rightarrow 2Li_2Si_2O_5 + Si. \qquad (2\text{-}1).^{42}$$

We confirmed that the SiO_2 matrix was amorphous (Figures 2-5 and 2-6); moreover, in this study, the SiO_2 matrix amorphized via MM presented a charge–discharge capacity.

that the capacities of the 1 wt.% Sn/SiO_2 and 3 wt.% Sn/SiO_2 electrodes were higher than that of the SiO_2 electrode. Furthermore, the discharge capacity and electronic conductivity of the y wt.% Sn/SiO_2 (y = 1, 3) electrodes increased with increasing the amount of Sn added to the SiO_2 matrix from 1 to 3 wt.% (Figure 2-4). Therefore, the discharge capacity of the SiO_2 electrode depended on the electronic conductivity of the SiO_2 powder. In other words, the reactivity of the SiO_2 matrix with Li-ions was improved by increasing the electronic conductivity of the SiO_2 matrix via the addition of Sn (Figure 2-9 (b)).

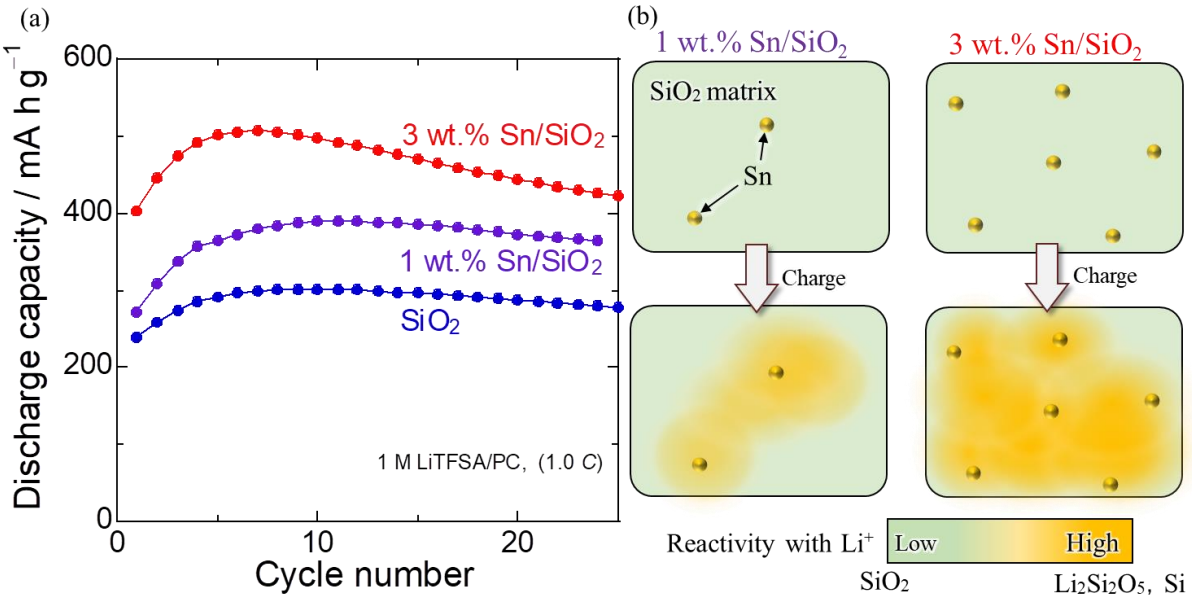

Figure 2-9. (a) Dependence of the discharge capacities of the SiO_2, 1 wt.% Sn/SiO_2, and 3 wt.% Sn/SiO_2 electrodes on the number of cycles in a 1 M LiTFSA solution in PC electrolyte (1.0 *C*). The temperature and potential range for the test were set to 303 K and 0.005–2.000 V vs. Li^+/Li, respectively. (b) Schematic of the reaction of the SiO_2 matrices of the 1 wt.% Sn/SiO_2 and 3 wt.% Sn/SiO_2 electrodes with Li-ions.

These results indicate that the addition of Sn to SiO_2 extended the cycle life of SiO_x. Si participated in the following two-step Li-ion occlusion reaction during charging:[43,44]

$$a\text{-Si} + 2Li^+ + 2e^- \rightarrow a\text{-}Li_{2.00}Si, \qquad (2\text{-}2)$$

$$a\text{-}Li_{2.00}Si + 1.75Li^+ + 1.75e^- \rightarrow c\text{-}Li_{3.75}Si, \qquad (2\text{-}3)$$

where *a* and *c* denote amorphous and crystalline, respectively.

The volume changes for the formation of $Li_{2.00}Si$ and $Li_{3.75}Si$ (Equations (2-2) and

(2-3), respectively), were 240 % and 380 %, respectively.[51] Therefore, as the reaction described by Equation (2-3) progressed, the electrodes disintegrated.

The SEM images of the electrodes tested under a limited charge capacity of 1000 mA h g(Si)$^{-1}$ (Figures 2-11 and 2-12) revealed that upon the uniform reaction of the elemental Si contained within the active material with Li, a $Li_{1.00}Si$ phase (theoretical capacity of 950 mA h g^{-1}) was primarily formed. However, as a result of actually analyzing the active material layer after charging and discharging, not only the $Li_{1.00}Si$ phase but also the Li–Si alloy phase with high Li concentration such as the $Li_{3.75}Si$ phase was formed. In addition, an unreacted crystalline Si phase remained. Our group has discovered these things so far. This is a result of using a conventional organic electrolyte, and it has been confirmed that when an ionic liquid is used as the electrolyte, the Li concentration becomes closer to homogeneous. In the organic electrolytic solution, a film having a non-uniform thickness is formed on the surface of the anode, so that Li storage in the active material layer proceeds preferentially from the place where the film is thin and the resistance is low. As a result, a $Li_{3.75}Si$ phase having a high Li concentration is formed on the electrolytic solution side. In addition, when cracks occur on the Si surface, a new surface that is not covered with a film appears. In that portion, a relatively thin film is formed, so that a phase having a high Li concentration is formed even in the middle of the Si layer. On the other hand, on the current collector side, a Li–Si alloy phase ($Li_{1.00}Si$ phase or $Li_{2.00}Si$ phase) having a low Li ratio may be formed, or unreacted Si

may remain. Therefore, it is inferred that the distribution of Li concentration in the Si layer became inhomogeneous. As a result, it has been reported that the strain accumulated locally in the electrode layer, causing the electrode to disintegration and the capacity to decay in a relatively short cycle.[44] Based on these results, the following considerations were made.

Figure 2-10 shows photographs of the external surfaces of the SiO_x, 1 wt.% Sn/SiO_x, 3 wt.% Sn/SiO_x, and 5 wt.% Sn/SiO_x electrodes before and after 300 cycles.

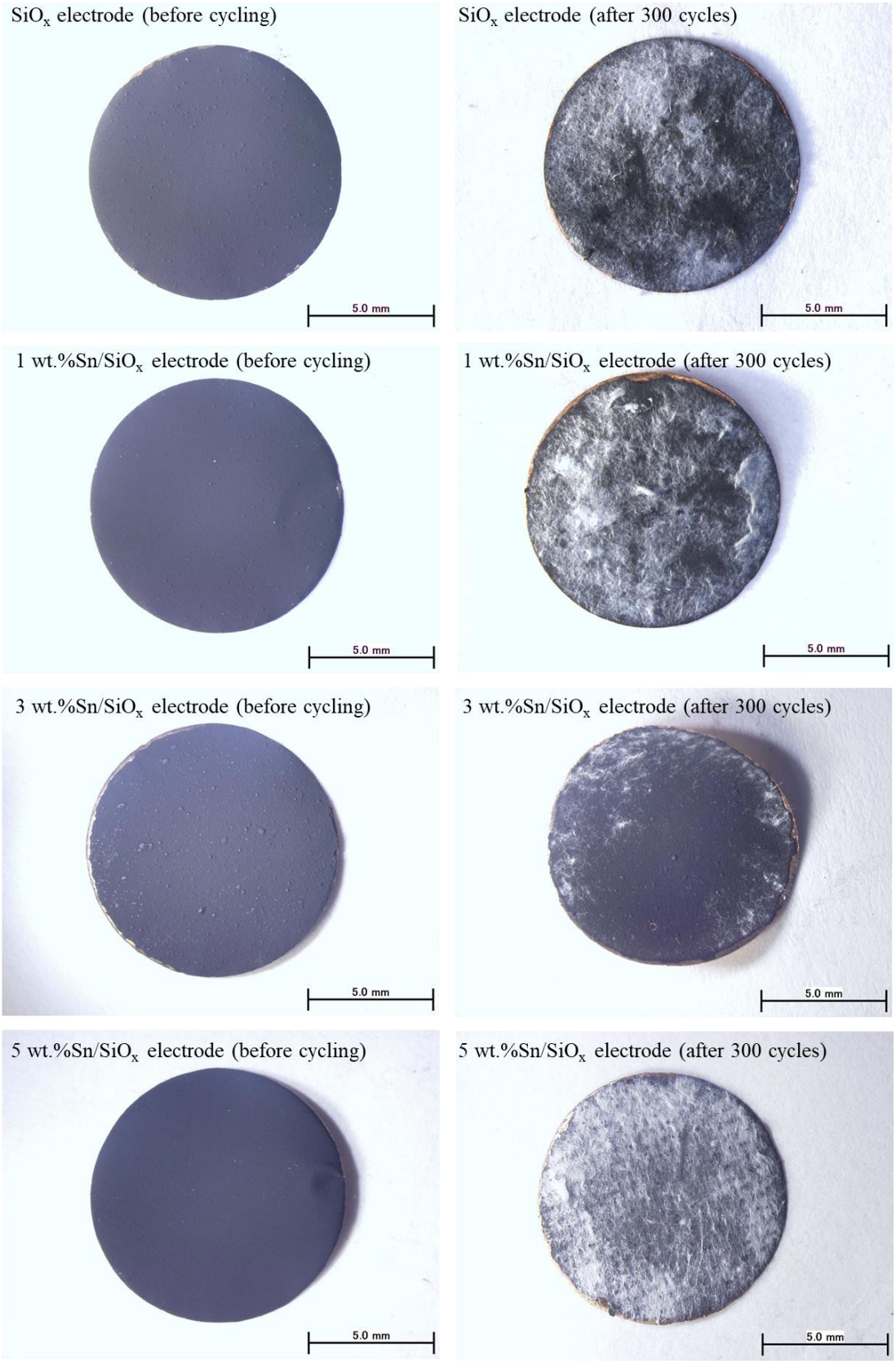

Figure 2-10. Photographs of the external appearance of the SiO_x, 1 wt.% Sn/SiO_x, 3 wt.% Sn/SiO_x, and 5 wt.% Sn/SiO_x electrodes before and after 300 cycles.

Figure 2-11 (a) and (b) show the SEM images of the surface of the 1 wt.% Sn/SiO_x electrode and schematic of the reaction mechanism of the electrode before and after charging–discharging. Numerous large cracks were observed on the surface of the 1 wt.% Sn/SiO_x electrode after cycling (Figure 2-11 (a)). Therefore, for the SiO_x and 1 wt.% Sn/SiO_x electrodes with no or a small Sn content, respectively, the Li-ion occlusion of Si occurred locally because of the low reactivity of the SiO_2 matrix with Li-ions (Figure 2-11 (b)). Consequently, a $Li_{3.75}Si$ phase with a large volume change formed, which was thought to have caused electrode disintegration and capacity decline (Figure 2-13).[45,46] Moreover, after cycling, the separator adhered to the surface of the 1 wt.% Sn/SiO_x electrode. This was attributed to the electrode pressing the separator owing to the large volume change of Si, causing the separator to sink into the surface layer of the electrode, further supporting the aforementioned conclusion. Similar results were obtained for the SiO_x electrode (Figure 2-14).

For the 5 wt.% Sn/SiO_x electrode, the metallic Sn that was not dissolved in the SiO_2 matrix formed agglomerates. The Si agglomerates presented a large electronic conductivity of 36×10^{-7} S cm^{-1} because they improved the electronic conductivity of SiO_x. However, we demonstrated that the discharge capacity of the 5 wt.% Sn/SiO_x electrode was comparable to that of the 3 wt.% Sn/SiO_x electrode (Figure 2-15). Therefore, Sn aggregates did not affect the Li-ion reactivity of the SiO_2 matrix. In other words, the Li-ion reactivities of the SiO_2

matrices of the 5 wt.% Sn/SiO_x and 3 wt.% Sn/SiO_x electrodes were comparable. However, the Sn aggregates in the SiO_2 matrix of the 5 wt.% Sn/SiO_x electrode reacted with Li, albeit only slightly (Figure 2-14). Consequently, it was hypothesized that the local volume change owing to the expansion and contraction of the Sn agglomerates that reacted with Li promoted crack formation (Figure 2-14).

Figure 2-12 (a) and (b) show the SEM images of the surface of the 3 wt.% Sn/SiO_x and schematic of the reaction mechanism of the electrode before and after charging–discharging. Unlike the surface of the 1 wt.% Sn/SiO_x electrode after cycling, that of the 3 wt.% Sn/SiO_x electrode did not present many large cracks after cycling. the electronic conductivity of the 3 wt.% Sn/SiO_x electrode was higher than that of the SiO_x electrode, and the Li-ion reactivity of the SiO_2 matrix was enhanced upon the addition of Sn to the SiO_2 matrix (Figure 2-12 (b)). This promoted the uniform occlusion of Li-ions by the Si in the active material layer. Therefore, the formation of $Li_{3.75}Si$ was suppressed, and the electrode experienced only a small volume change (Figure 2-13). Consequently, the stress induced by the volume expansion of Si could not accumulate, the damage to the electrodes was small, electrode disintegration was suppressed, which improved the cycle properties of the electrode. In addition, it was considered that the damage to the electrodes caused by the formation of $Li_{1.00}Si$ and $Li_{2.00}Si$ phases was relatively small. This was attributed to the expansion rates of $Li_{1.00}Si$ and $Li_{2.00}Si$ for the Si electrode being 125 % and 240 %, respectively, which were

smaller than the expansion rate of $Li_{3.75}Si$ of 380 %. Moreover, the Li-ion storage capacities of Sn for the 1 wt.% Sn/SiO_x and 3 wt.% Sn/SiO_x electrodes with small Sn contents were negligible. Therefore, the effect of Sn on the electrochemical reaction was negligible. Consequently, it was considered that the primary role of Sn was to improve the electronic conductivity of the active material layer.

Furthermore, the separator did not adhere to the 3 wt.% Sn/SiO_x electrode. This was attributed to the formation of a $Li_{2.00}Si$ phase with a small expansion rate. Consequently, the electrode did not press the separator because the volume change of Si was suppressed.

These results suggested that the optimum Sn content that would improve the cycle performance of SiO_x was ~ 3 wt.%.

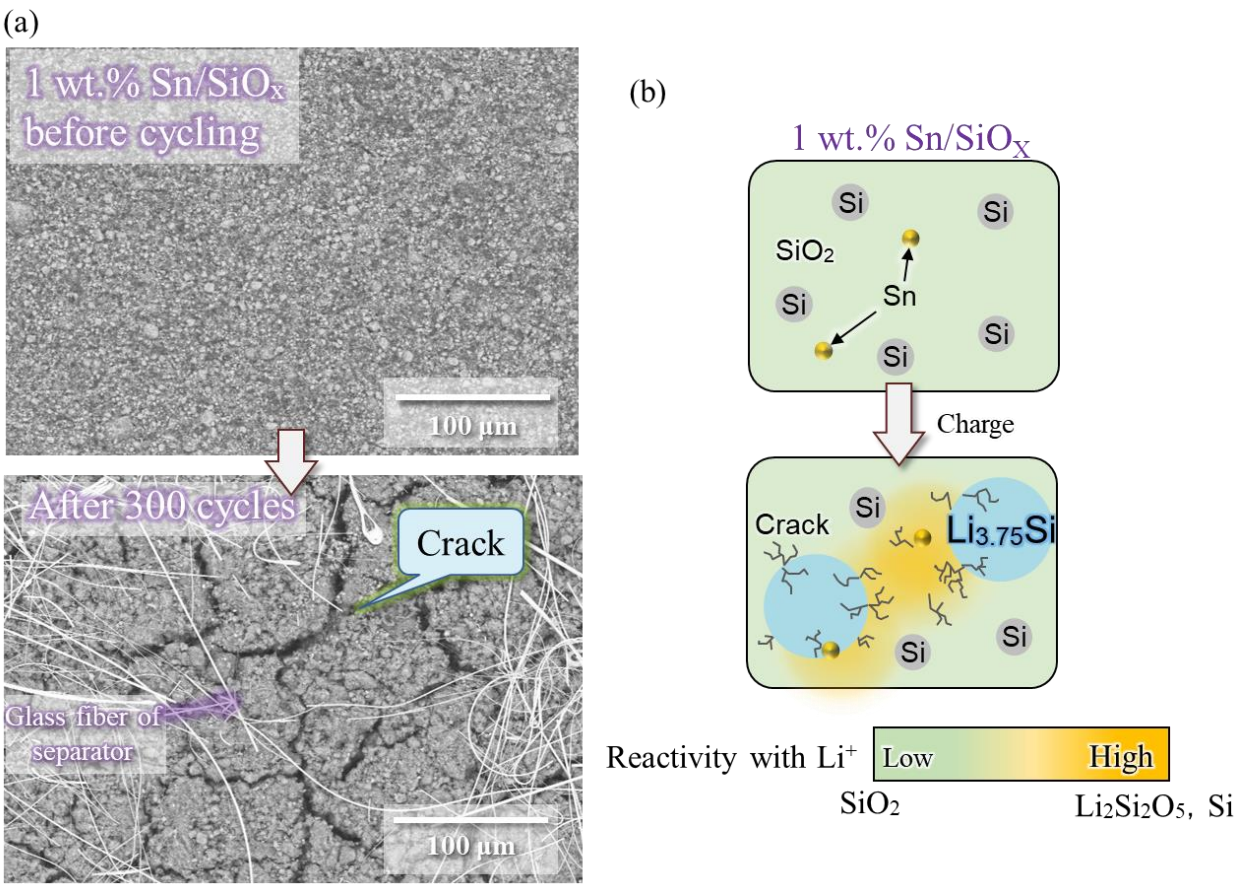

Figure 2-11. (a) SEM images of a 1 wt.% Sn/SiO_x electrode before and after 300 cycles and (b) Schematic of the reaction mechanism of the 1 wt.% Sn/SiO_x electrode.

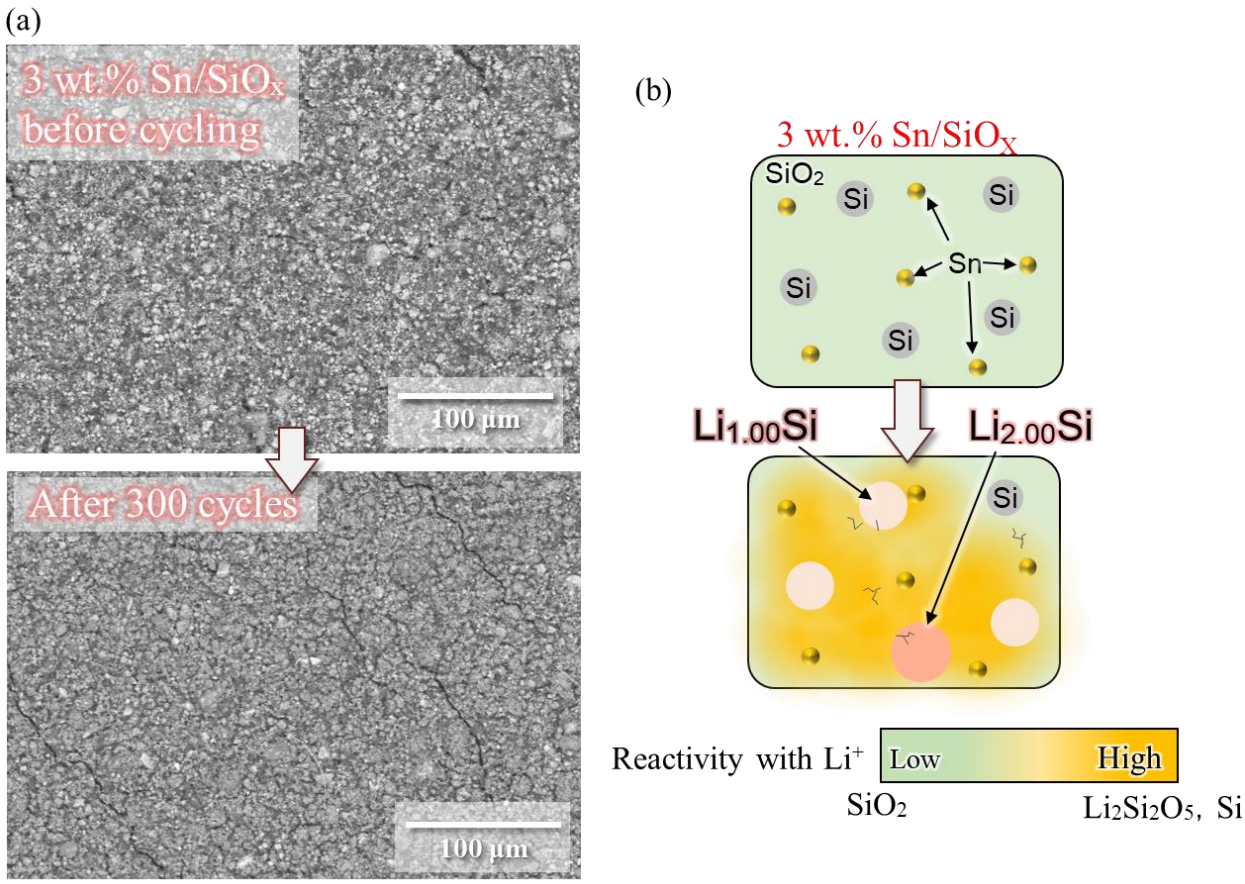

Figure 2-12. (a) SEM images of a 3 wt.% Sn/SiO_x electrode before and after 300 cycles and (b) Schematic of the reaction mechanism of the 3 wt.% Sn/SiO_x electrode.

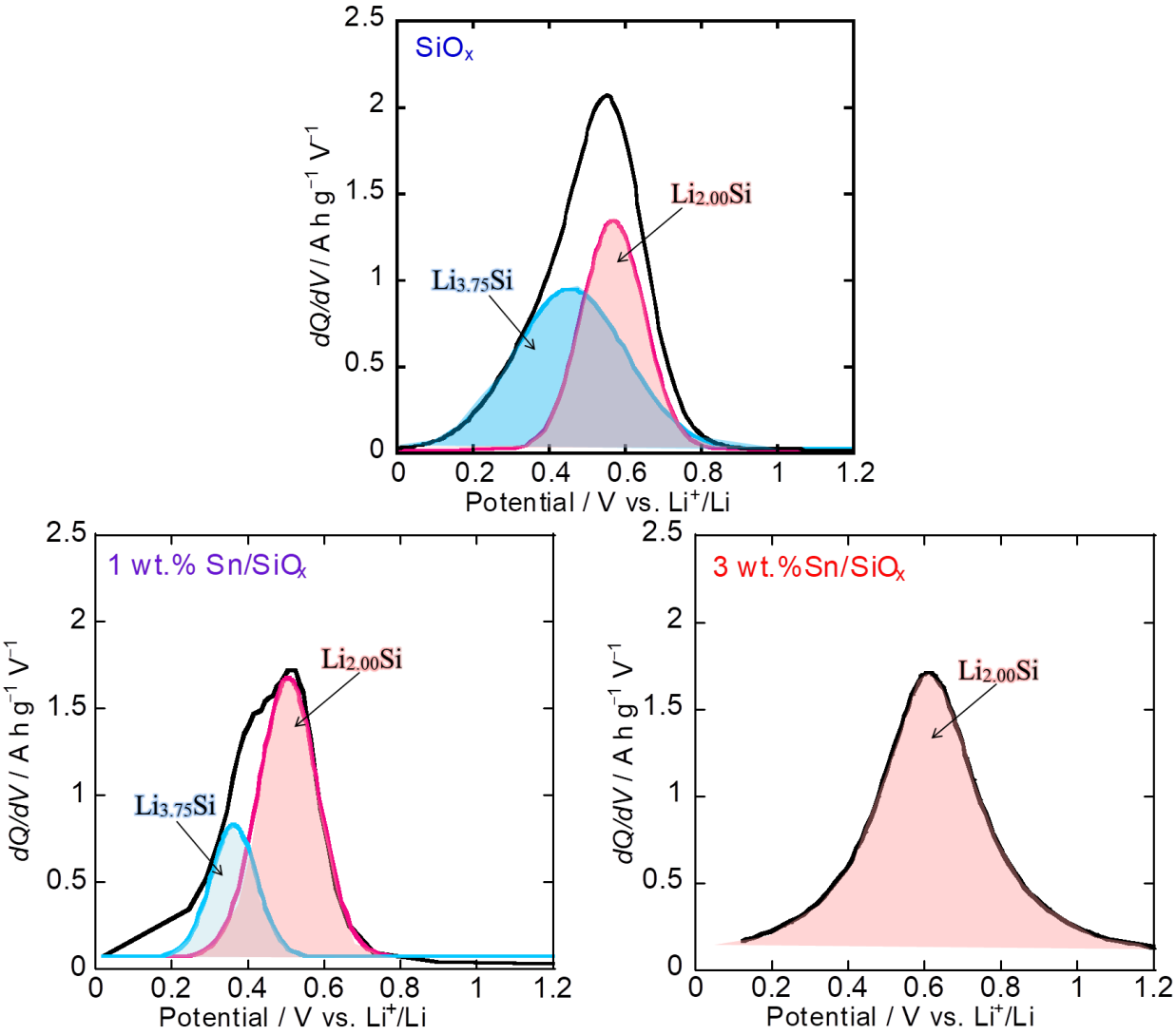

Figure 2-13. dQ/dV plots of the SiO_x, 1 wt.% Sn/SiO_x, and 3 wt.% Sn/SiO_x electrodes in a 1 M LiTFSA solution in PC as the electrolyte after 200 cycles.

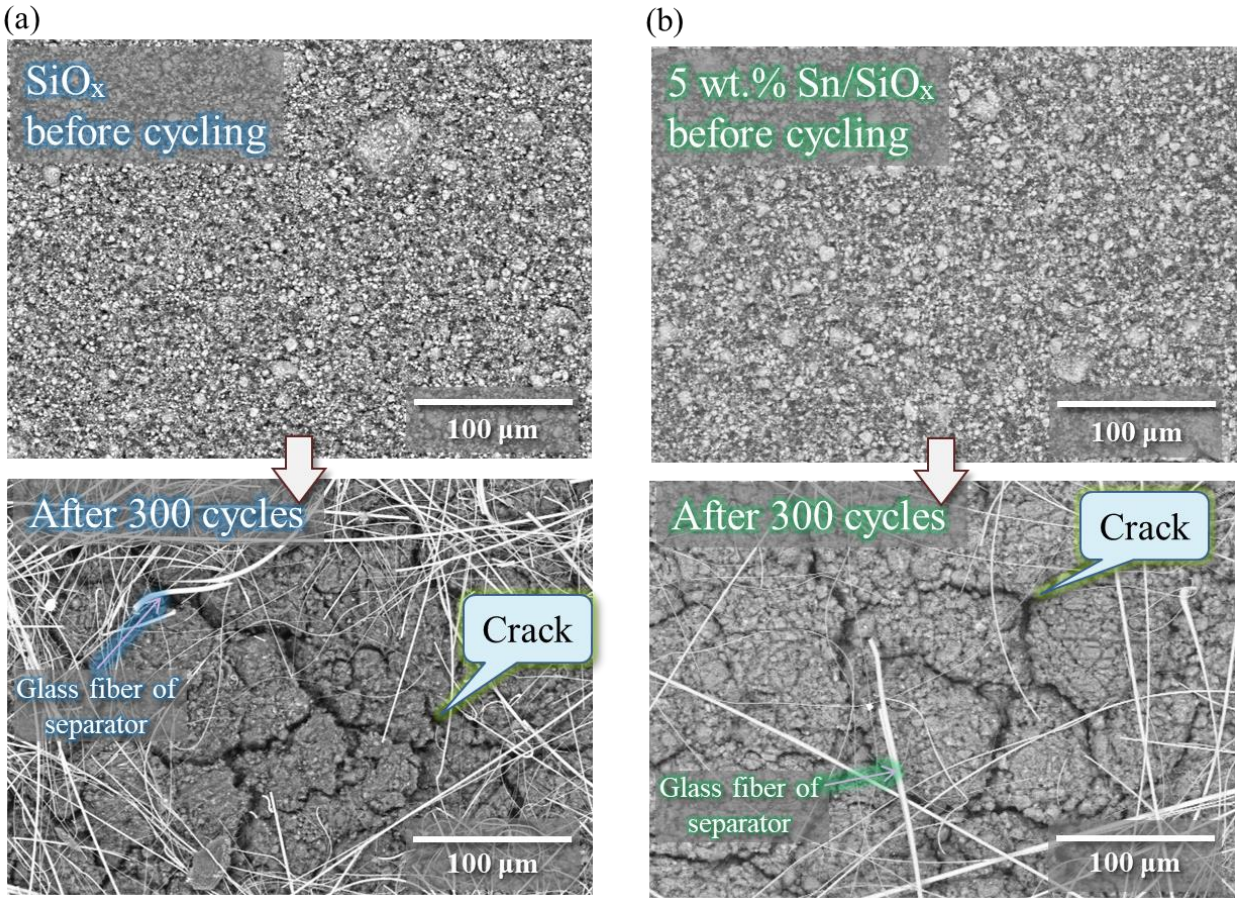

Figure 2-14. SEM images of (a) SiO_x and (b) 5 wt.% Sn/SiO_x electrodes before and after 300 cycles.

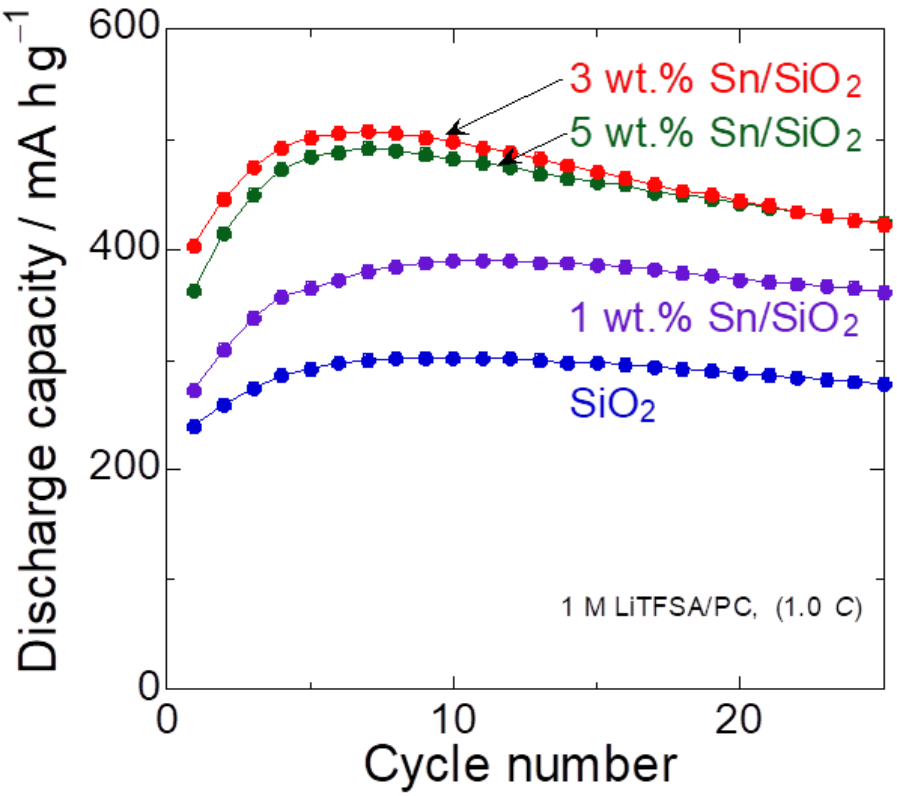

Figure 2-15. Dependence of the discharge capacity of the SiO_2, 1 wt.% Sn/SiO_2, 3 wt.% Sn/SiO_2, and 5 wt.% Sn/SiO_2 electrodes on the cycle number in a 1 M LiTFSA solution in PC (1.0 *C*) as the electrolyte.

2.4 Summary

In this study, we investigated the effect of the amount of Sn on the properties and cycle life of y wt.% Sn/SiO_x (y = 1, 3, and 5) anode materials. During a cycle test in which the Li insertion amount was regulated at 1000 mA h g^{-1}, the discharge capacity of the SiO_x electrode declined rapidly over 170 cycles. Conversely, the discharge capacities of the 1 wt.% Sn/SiO_x, 3 wt.% Sn/SiO_x were maintained for 250 and 360 cycles, respectively, and the charge–

discharge cycle life of the electrodes was extended with increasing amount of Sn. Furthermore, at a Li insertion amount of 750 mA h g^{-1}, the difference between the cycle life of the SiO_x and 1 or 3 wt.% Sn/SiO_x electrodes was considerably higher than that at a Li insertion amount of 1000 mA h g^{-1}. Furthermore, the discharge capacity of the 3 wt.% Sn/SiO_x electrode was maintained for 540 cycles. These results confirmed the effect of Sn addition on the performance of the y wt.% Sn/SiO_x (y = 1, 3, and 5) electrodes.

For the 1 wt.% Sn/SiO_x electrode with a small Sn content, Si occluded Li-ions locally because of the low reactivity of the SiO_2 matrix with Li-ions. Consequently, $Li_{3.75}Si$ with a large expansion rate formed, which was thought to have caused electrode disintegration and capacity decline. Conversely, the electronic conductivity of the 3 wt.% Sn/SiO_x electrode was higher than that of the SiO_x electrode and the Li-ion reactivity of the SiO_2 matrix was higher than that of the SiO_2 matrix of the SiO_x electrode. This promoted the uniform occlusion of Li-ions by the Si in the active material layer. Therefore, the stress induced by the volume expansion of Si could not accumulate, the damage to the electrodes was negligible, and electrode disintegration was suppressed, which improved the cycle properties of the electrode. In other words, an electrode with a long lifetime was fabricated.

Chapter 3

Effect of Sn Addition on the Anode Properties of SiO_x for Sodium-Ion Batteries

3.1 Introduction

Currently, secondary batteries, including Li-ion batteries, can store renewable energy and can be used repeatedly without emitting CO_2. Therefore, a low-carbon society can be achieved. Furthermore, Li-ion batteries have attracted increasing attention as devices that can contribute to achieving a sustainable society because they do not contain Cd or Pb and have low environmental impact. In particular, Li-ion batteries are widely used as power sources for mobile phones and laptop computers. Li-ion batteries have recently been used as power sources for electric and hybrid vehicles, or stationary power sources, and the demand for Li-ion batteries has increased rapidly. However, Li is a scarce resource, and its extraction is limited to some regions overseas. Consequently, a stable Li supply cannot be achieved from resource and cost perspectives.

Conversely, Na-ion batteries charge and discharge by transferring Na ions between the cathode and anode. In the concentration of Na in seawater is high; therefore, Na is an abundant resource and a stable supply can be achieved from resource and cost perspectives.

Na ions are more than three times larger than Li-ions. Consequently, the anode materials used for conventional Li-ion batteries can hinder the charge–discharge reaction of Na-ion batteries. Currently, carbon-based materials, such as hard carbon, with capacities of the order of 400 mA h g^{-1} are used as anode materials for Na-ion batteries. However, the low capacity of carbon-based anode materials limit the applications of Na-ion batteries. Therefore, the development of anode materials that can occlude abundant Na-ions is critical.[52,53]

For example, the theoretical capacities of Na-storage elements such as P, Sn, and Sb are high (2596, 847, and 660 mA h g^{-1}, respectively). However, once the anode material occludes Na-ions, the material expands to more than five times its original volume. Consequently, the structure of the anode collapses. We determined that tin phosphide (Sn_4P_3) reversibly stores abundant Na-ions and has excellent cycle life. Furthermore, we elucidated the mechanism responsible for the high capacity and long cycle life of Sn_4P_3.[54–56] In addition, we fabricated several new materials,[57–59] such as tin compounds,[60,61] silicon oxide,[17] phosphides,[62] and Sb alloys.[63]

Moreover, we demonstrated that Sn/SiO_x materials exhibited excellent properties as anode materials for Li-ion batteries.[50,64] Upon dispersing Sn in SiO_2 matrices, the electron conductivity of SiO_2 was increased, and SiO_2 could store and release Li-ions more uniformly. Consequently, the stress caused by the volume change of Si could not accumulate, and electrode collapse was hindered.[50] We considered that the same process occurs for the anode

materials of Na-ion batteries. In addition, to the best of our knowledge, the development and use of Sn/SiO_x as an anode material for Na-ion batteries has not yet been studied. Furthermore, the applications of Sn/SiO_x materials can expand beyond their use as anode materials for Li- and Na-ion batteries and there will be merits in terms of cost.

In this study, we investigated the possibility of using Sn/SiO_x as anode materials for Na-ion batteries, and evaluated the effects of the addition of Sn on the properties of Sn/SiO_x anode materials.

3.2 Experimental

3.2.1 Preparation of SiO_x and Sn/SiO_x (Sn content = 1, 3, and 5 wt.%) powders

Si powder was prepared using a mass-produced gas atomizer according to a previously described procedure.[50]

To prepare SiO_x powder, gas-atomized Si powder (32.4 g) and commercially available SiO_2 powder (27.6 g; purity 99.9 %) were mixed at a mass ratio of 54:46. The mixture was added to an austenite stainless-steel vessel filled with crushed Φ19 mm high-carbon chromium-bearing steel (C 1 wt.%, Cr 1 wt.%) balls with the total mass of 12 kg The active-material–to–balls mass ratio was 1:200.

The method used to fabricate SiO_x powder was utilized to prepare y wt.% Sn/SiO_x (y =

1, 3, and 5) powders. The 1 wt.% Sn/SiO_x powder was fabricated using 32.1 g of Si powder, 27.3 g of SiO_2 powder, and 0.6 g of Sn powder. The 3 wt.% Sn/SiO_x powder was synthesized using 31.4 g of Si powder, 26.8 g of SiO_2 powder, and 1.8 g of Sn powder. The 5 wt.% Sn/SiO_x powder was manufactured using 30.8 g of Si powder, 26.2 g of SiO_2 powder, and 3.0 g of Sn powder.

The vessels containing the powder mixtures were sealed, evacuated to a pressure of 0.1 MPa, and then dry Ar gas was filled by gas replacement. Each vessel was attached to a vibrating ball mill (MB-1, Chuo Kakohki Co.), and MM was performed for 14 h under an amplitude of ± 4 mm and at a frequency of 1200 rpm). Thereafter, the number of balls was increased, such that the active materials-to-crushed balls mass ratio was 1:300, and MM was performed for 14 h.

The particle size of the as-obtained MM powder was adjusted to ≤ 10 μm using a jet mill (Co-Jet, Seishin Enterprise Co., Ltd.), which crushed the agglomerated powder via a collision between the powder particles under a 0.7 MPa N_2 gas stream.

Samples of the obtained powders (1.5 g) were sealed in zirconia grinding container with grinding balls (Φ5 mm, total mass of 100 g), which was placed in a PL-7 premium line planetary ball mill. The samples were mechanically milled at 380 rpm for 20 h to obtain the target samples.

3.2.2 Analysis of the as-obtained powders

The electrode cross sections before and after charging–discharging were analyzed using a TEM (JEM-F200, JEOL Ltd.) instrument operated at 200 kV. To prepare the samples for TEM analysis, each prepared powder sample was embedded in a conductive thermosetting resin, and then a carbon protective film was deposited on the sample surface. Lastly, these samples were cut into ~10 μm × 10 μm × 100 nm specimens using a high-performance focused ion beam device (MI4050, Mo mesh, Hitachi High-Tech Corp.).

3.2.3 Electrode preparation

A Cu foil substrate was placed in the chamber and the pressure was decreased. Next, the powder was aerosolized using He gas at a pressure of 0.7 MPa and ejected from a nozzle to form a film comprising only the active material onto the Cu foil substrate.

3.2.4 Cell assembly and charge–discharge tests

The 2032-type coin cells used for charge–discharge tests comprised the aforementioned electrodes as the working electrodes, a Na metal sheet as the counter electrode, and a glass fiber filter as the separator. A 1 M solution of sodium bis(fluorosulfonyl) amide (NaFSA) in

PC was used as the electrolyte.

The SiO_x, 1 wt.% Sn/SiO_x, 3 wt.% Sn/SiO_x, and 5 wt.% Sn/SiO_x electrodes, were subjected to galvanostatic charge–discharge cycling tests using an electrochemical measurement system in the potential range of 0.005–3.000 V vs. Na^+/Na. The current density and temperature were set to 50 mA g^{-1} (0.1 *C*) and 303 K, respectively.

3.3 Results and Discussion

Because the samples were prepared via MM, Sn could have reacted with the raw material powder or dissolved in Si owing to the high energy generated during the collision of the high-carbon chromium-bearing steel balls with each other or the powder. According to previous studies on anode materials for Li-ion batteries, cluster-like Si was dispersed throughout the SiO_2 matrix in which Sn was dispersed regardless of the Sn content.[50,64]

We have previously reported that the discharge capacity of SiO electrodes for Na-ion batteries increased with decreasing Si crystallite size.[17] Multiple particles were present in the TEM images of 3 wt.% Sn/SiO_x electrodes. This was supported by the halos observed in the electron diffraction patterns of 3 wt.% Sn/SiO_x electrodes indicating that an amorphous material was obtained (Figure 3-1). No Si microcrystals were observed, and the structure of the 3 wt.% Sn/SiO_x electrodes was amorphous.

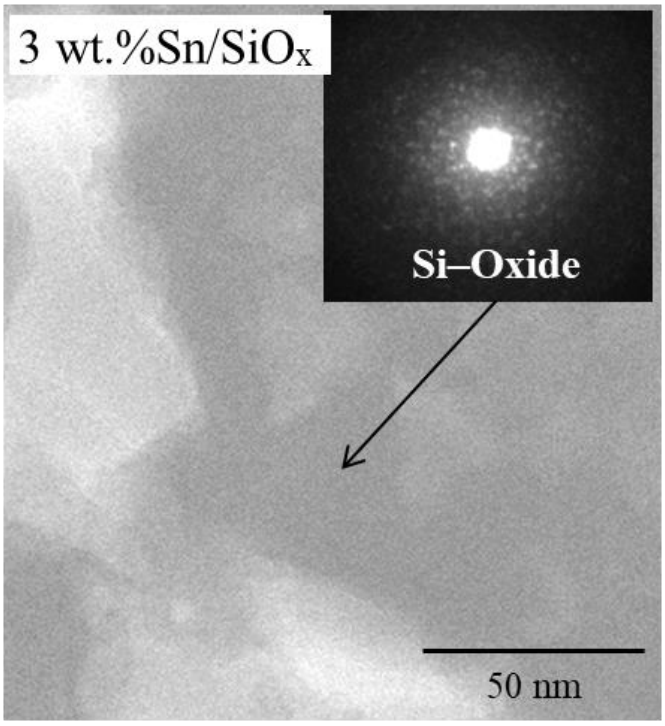

Figure 3-1. TEM image and the electron diffraction pattern (inset) of as-prepared 3 wt.% Sn/SiO_x powder.

Figure 3-2 shows changes in the discharge (Na desorption) capacities of SiO_x, 1 wt.% Sn/SiO_x, 3 wt.% Sn/SiO_x, and 5 wt.% Sn/SiO_x electrodes. The discharge capacity of the SiO_x electrode was only 300 mA h $g(Si)^{-1}$. The discharge capacities of the 1 wt.% Sn/SiO_x and 5 wt.% Sn/SiO_x electrodes were comparable to that of the SiO_x electrode. However, the discharge capacity of the 3 wt.% Sn/SiO_x electrode was higher (600 mA h $g(Si)^{-1}$), and it was maintained for 140 cycles.

These results indicate that y wt.% Sn/SiO_x (y = 1, 3, and 5) can be used as anode materials for Li- and Na-ion batteries.

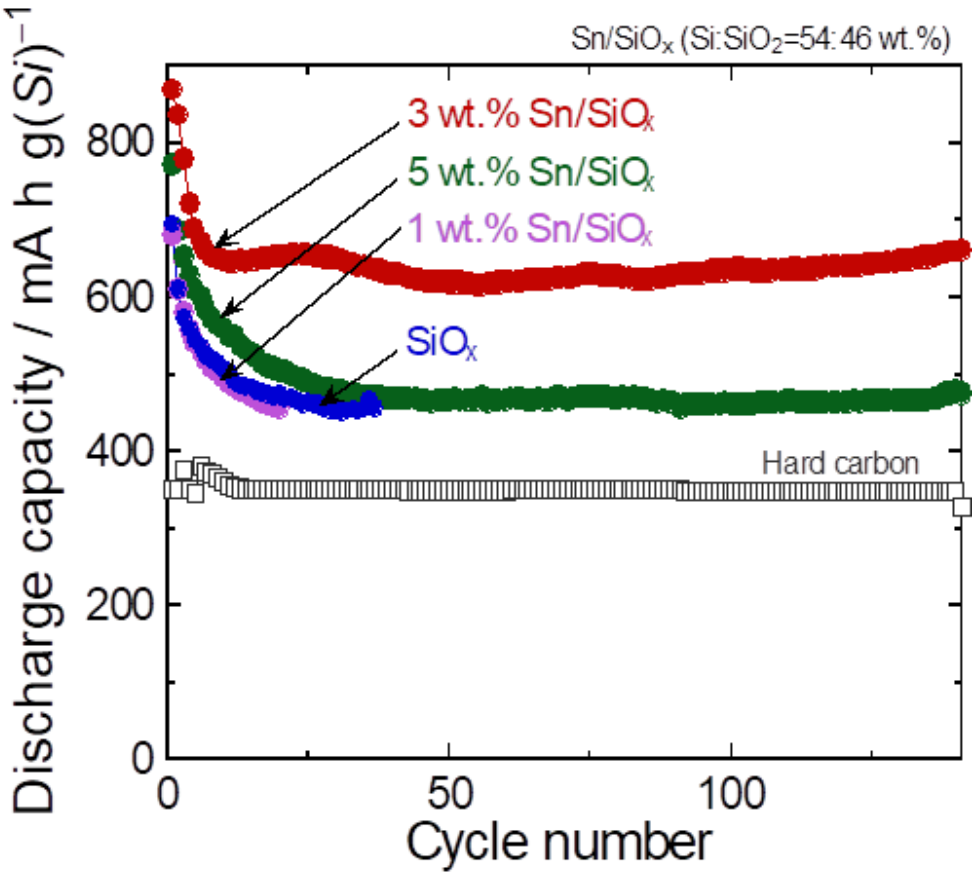

Figure 3-2. Dependence of the discharge capacity of hard carbon, SiO_x, 1 wt.% Sn/SiO_x, 3 wt.% Sn/SiO_x, and 5 wt.% Sn/SiO_x electrodes on the cycle number in a 1 M NaFSA solution in PC as the electrolyte.

To investigate this factor, we fabricated a SiO_2 electrode, and evaluated its reactivity with Na-ions. Figure 3-3 shows the changes in the discharge (Na desorption) capacities of y wt.% Sn/SiO_2 (y = 1, 3, and 5) electrodes. The only electrode with a capacity higher than that of the SiO_2 electrode was the 3 wt.% Sn/SiO_2 electrode. Therefore, it was concluded that the addition of 3 wt.% Sn to SiO_2 improved the reactivity of SiO_2 with Na-ions. These results suggest that the addition of Sn to SiO_2 improved the Na-ion conductivity of SiO_2, promoting

the movement of Na-ions toward the Si clusters and increasing the utilization of Si, thereby resulting in a high discharge capacity.

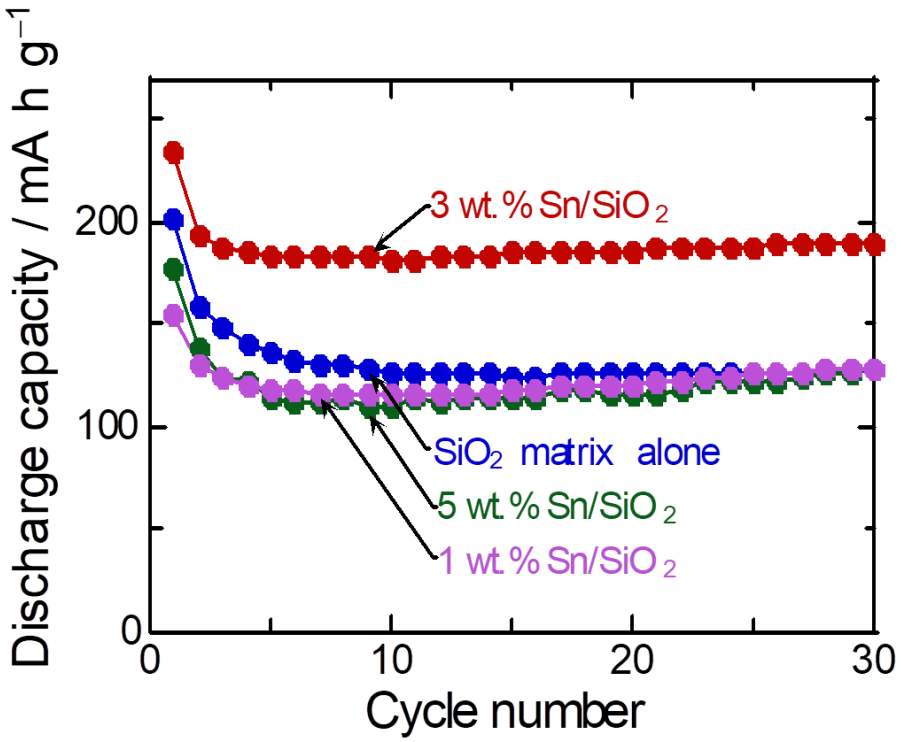

Figure 3-3. Cycle performances of SiO_2 and y wt.% Sn/SiO_2 (y = 1, 3, and 5) electrodes in a 1 M NaFSA solution in PC as the electrolyte.

The cycle performance of the SiO_x and 3 wt.% Sn/SiO_x electrodes deteriorated after 10 cycles. This tendency was more pronounced for the SiO_x electrode.

The cross-sectional TEM images of the SiO_2 and 3 wt.% Sn/SiO_2 electrodes were used to investigate the cause for the decline in electrode cycle performance (Figure 3-4). For the SiO_x electrode, the active material layer was thin and uniform before charging–discharging. However, after 10 cycles, the active material swelled partially and a highly non-uniform

active material layer was formed. Furthermore, delamination was observed between the active material layer and Cu substrate. Conversely, for the 3 wt.% Sn/SiO_x electrode, the active material layer did not change, and it did not separate from the Cu substrate as much as the active material layer of the SiO_x electrode did.

These findings indicate that for the SiO_x electrode, the reaction of Na-ions with the SiO_2 matrix was non-uniform and the local electrode reaction proceeded. Consequently, the expansion rate of Si in a fraction of the active material layer was high, and the active material delaminated from the Cu substrate, causing the cycle properties of the SiO_x electrode to deteriorate. Conversely, for the 3 wt.% Sn/SiO_x electrode, the reaction of Na-ions with the SiO_2 matrix was uniform, and the reaction was uniform throughout the electrode. Consequently, the active material did not separate from the Cu substrate owing to volume change caused by the expansion and contraction of Si, and a conductive pathway was maintained. Therefore, the cycle properties of the 3 wt.% Sn/SiO_x electrode were excellent.

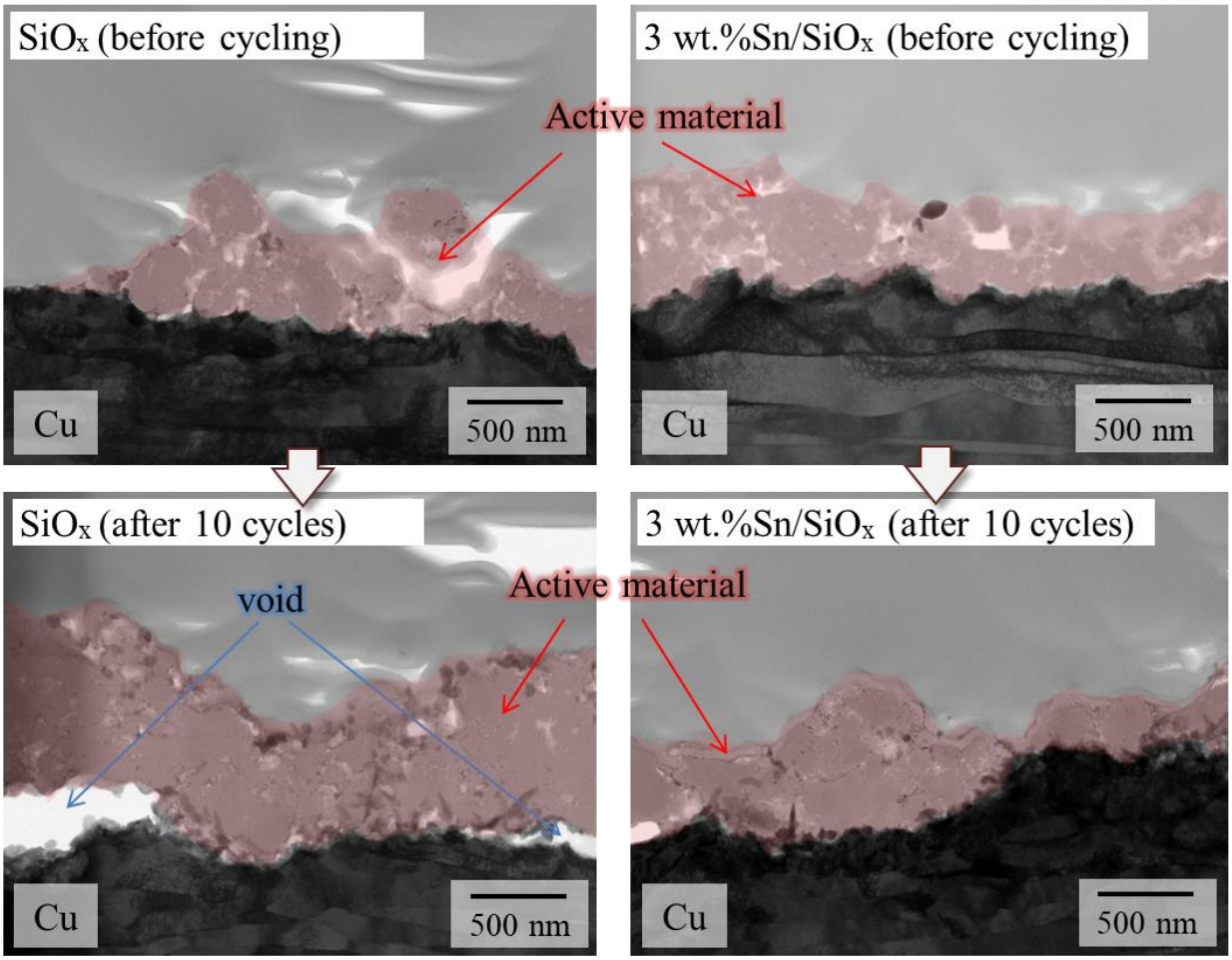

Figure 3-4. Cross-sectional TEM images of SiO_x and 3 wt.% Sn/SiO_x electrodes before and after 10 cycles.

3.4 Summary

In this study, we investigated the possibility of using Sn/SiO_x as a anode materials for Na-ion batteries. The results of the charge–discharge cycle tests indicate that the discharge capacity of the 3 wt.% Sn/SiO_x electrode exceeded that of the commonly used hard carbon anode during long cycling. The reaction of Na^+ within the SiO_2 matrix of the SiO_x electrode

was non-uniform and a local electrode reaction proceeded. Consequently, a large volume expansion of Si occurred in a fraction of the active material layer, and the active material delaminated from the Cu substrate, causing the cycle properties of the SiO_x electrode to deteriorate. Conversely, for the 3 wt.% Sn/SiO_x electrode, the reaction of Na-ions with the SiO_2 matrix was uniform, and the reaction was uniform throughout the electrode. Consequently, the active material did not separate from the Cu substrate owing to volume changes caused by the expansion and contraction of Si, and a conductive pathway was maintained. Therefore, the cycle properties of the 3 wt.% Sn/SiO_x electrode were excellent.

These results indicate that y wt.% Sn/SiO_x (y = 1, 3, and 5) can be used as anode materials for Li- and Na-ion batteries.

Concluding Remarks

In this study, we investigated a new method for improving the properties of SiO_x anode material by increasing the low electronic conductivity of the SiO_2 matrix using an MM method that promoted development of various material designs.

1. *M*/SiO_x (*M* = Sn, B, Al) active materials were prepared using an MM method and their lithiation and delithiation properties were evaluated. The cycling lives of the B/SiO_x and Sn/SiO_x electrodes were longer than that of the SiO_x electrode owing to their high electronic conductivities. We consider that the increase in electronic conductivity of SiO_2 promoted the uniform reaction of SiO_x with Li-ions. It was concluded that this prevented concentration of the stress induced by the volume changes of Si and suppressed electrode disintegration.

2. We have previously demonstrated that cycling life of Sn/SiO_x as an anode for Li-ion batteries was higher than that of SiO_x because Sn addition increased the electronic conductivity of the SiO_2 matrix of SiO_x. In this study, we investigated the effect of the amount of added Sn on the performance of the Sn/SiO_x anode. The cycling life of the Sn/SiO_x electrodes increased with increasing Sn amount. We confirmed that the electronic conductivity and Li reactivity of SiO_2 increased with increasing Sn amount. Therefore, it was suggested that the addition of Sn to SiO_x promoted the uniform reaction of the Si clusters present in the SiO_x matrix with Li-ions, hindering stress concentration and preventing electrode disintegration.

3. We also used Sn/SiO_x as an anode material for Na-ion batteries. The charge–discharge tests revealed that the discharge capacity of the Sn/SiO_x anode material with a Sn content of 3 wt.% exceeds that of the commonly used hard carbon anode during long cycling. Consequently, for the 3 wt.% Sn/SiO_x electrode, the reaction of Na-ions with the SiO_2 matrix was uniform, and the reaction was uniform throughout the electrode. Accordingly, the active material did not separate from the Cu substrate owing to volume changes induced by the expansion and contraction of Si, and a conductive pathway was maintained. Therefore, the cycle properties of the 3 wt.% Sn/SiO_x electrode were excellent. Moreover, we determined that Sn/SiO_x can be used as an anode material for Li- and Na-ion batteries.

Acknowledgements

The author expresses his sincere gratitude to Professor Hiroki Sakaguchi at the Department of Chemistry and Biotechnology, Graduated School of Engineering, Tottori University, for his passionate guidance, invaluable suggestions, and encouragement throughout this study.

The author would also like to thank Associate Professor Hiroyuki Usui for his appropriate suggestions, gentle coaching, and helpful discussions.

The author is grateful to Associate Professor Yasuhiro Domi for his polite guidance, precise correction of our manuscripts, and excellent advice.

Special thanks to Wataru Irie and Takahiro Nishida and all other staff at the laboratory of Professor Hiroki Sakaguchi for their supports and warm welcome.

The author would like to express my sincere gratitude to Managing Director Katsu Yanagimoto for providing me this opportunity and understanding in obtaining my Ph.D. And, I would also like to express my sincere gratitude to Masatoshi Yamamoto, General Manager of the Powder Division, for his understanding of my experiments and research. Also, the author wishes to thank Yoshikazu Aikawa, Hiroki Ikeda, Toshiyuki Sawada for giving useful advice for experiments. In addition, I would also like to express my sincere gratitude to everyone in the Testing and Research Section of Sanyo Special Steel Co., Ltd. for their constant support of our experiments.

Lastly, the author gratefully thanks my wife, Hiroko, son, Haruki, and daughter, Mitsuki for their unconditional support.

References

[1] P. Zuo, G. Yin, X. Hao, Z. Yang, Y. Ma, and Z. Gao, *Mater. Chem. Phys.* **104** (2007) 444.

[2] H. Sakaguchi, T. Iida, M. Itoh, N. Shibamura, and T. Hirono, *IOP Conf. Ser. Mat. Sci. Eng.* **1** (2009) 012030.

[3] H. Usui, M. Shibata, K. Nakai, and H. Sakaguchi, *J. Power Sources* **196** (2011) 2143.

[4] H. Usui, H. Nishinami, T. Iida, and H. Sakaguchi, *Electrochemistry* **78** (2010) 329.

[5] H. Usui, N. Uchida, and H. Sakaguchi, *J. Power Sources* **196** (2011) 10244.

[6] H. Usui, K. Meabara, K. Nakai, and H. Sakaguchi, *Int. J. Electrochem. Sc.* **6** (2011) 2246.

[7] H. Usui, M. Shimizu, and H. Sakaguchi, *J. Power Sources* **235** (2013) 29.

[8] H. Usui, N. Uchida, and H. Sakaguchi, *Electrochemistry* **80** (2012) 737.

[9] H. Usui, M. Nomura, H. Nishino, M. Kusatsu, T. Murota, and H. Sakaguchi, *Mater. Lett.* **130** (2014) 61.

[10] Y. Domi, H. Usui, H. Itoh, and H. Sakaguchi, *J. Alloys Compd.* **695** (2017) 2035.

[11] Y. Domi, H. Usui, A. Ueno, Y. Shindo, H. Mizuguchi, T. Komura, T. Nokami, T. Itoh, and H. Sakaguchi, *J. Electrochem. Soc.* **167** (2020) 040512.

[12] Y. Domi, H. Usui, K. Sugimoto, and H. Sakaguchi, *Energy Technology* **7** (2019) 1800946.

[13] K. Yamaguchi, Y. Domi, H. Usui, M. Shimizu, S. Morishita, S. Yodoya, T. Sakata, and H. Sakaguchi, *J. Electrochem. Soc.* **166** (2019) A268.

[14] T. Iida, T. Hirono, N. Shibamura, and H. Sakaguchi, *Electrochemistry* **76** (2008) 644.

[15] H. Usui, K. Nouno, Y. Takemoto, K. Nakada, A. Ishii, and H. Sakaguchi, *J. Power Sources* **268** (2014) 848.

[16] Y. Nagao, H. Sakaguchi, H. Honda, T. Fukunaga, and T. Esaka, *J. Electrochem. Soc.* **151** (2004) A1572.

[17] M. Shimizu, H. Usui, K. Fujiwara, K. Yamane, and H. Sakaguchi, *J. Alloys Compd.* **640** (2015) 440.

[18] J. Yang, Y. Takeda, N. Imanishi, C. Capiglia, J. Y. Xie, and O. Yamamoto, *Solid State Ionics* **152–153** (2002) 125.

[19] M. Miyachi, H. Yamamoto, H. Kawai, T. Ohta, and M. Shirakata, *J. Electrochem. Soc.* **152** (2005) A2089.

[20] M. Miyachi, H. Yamamoto, and H. Kawai, *J. Electrochem. Soc.* **154** (2007) A376.

[21] M. A. Al-Maghrabi, J. Suzuki, R. J. Sanderson, V. L. Chevrier, R. A. Dunlap, and J. R. Dahn, *J. Electrochem. Soc.* **160** (2013) A1587.

[22] T. Chen, J. Wu, Q. Zhang, and X. Su, *J. Power Sources* **363** (2017) 126.

[23] H. C. Tao, X. L. Yang, L. L. Zhang, and S. B. Ni, *Mater. Chem. Phys.* **147** (2014) 528.

[24] T. Zhang, J. Gao, H. P. Zhang, L. C. Yang, Y. P. Wu, and H. Q. Wu, *Electrochem. Commun.* **9** (2007) 886.

[25] J. Lee, J. Koo, B. Jang, and S. Kim, *J. Power Sources* **329** (2016) 79.

[26] J. Choi, M. J. Lee, S. M. Oh, and J. J. Kim, *Electrochim. Acta* **85** (2012) 369.

[27] A. Hirata, S. Kohara, T. Asada, M. Arao, C. Yogi, H. Imai, Y. Tan, T. Fujita, and M. Chen, *Nat. Commun.* **7** (2016) 11591.

[28] K. Yasuda, Y. Kashitani, S. Kizaki, K. Takeshita, T. Fujita, and S. Shimosaki, *J. Power Sources* **329** (2016) 462.

[29] Y. Domi, H. Usui, Y. Takemoto, K. Yamaguchi, and H. Sakaguchi, *J. Phys. Chem. C.* **120** (2016) 16333.

[30] S. C. Hou, Y. F. Su, C. C. Chang, C. W. Hu, T. Y. Chen, S. M. Yang, and J. L. Huang, *J. Power Sources* **349** (2017) 111.

[31] H. Usui, K. Wasada, M. Shimizu, and H. Sakaguchi, *Electrochim. Acta* **111** (2013) 575.

[32] H. Usui, Y. Kashiwa, T. Iida, and H. Sakaguchi, *J. Power Sources* **195** (2010) 3649.

[33] Y. Domi, H. Usui, Y. Shindo, A. Ando, and H. Sakaguchi, *Chem. Lett.* **50** (2021) 1041.

[34] D. Jian, T. Xuan, D. Haifeng, Y. Ying, W. Wangyan, W. Xuezhe, and H. Yunhui, *Electrochem. Energy Rev.* **3** (2020) 1.

[35] X. Fengxia and W. M. Stanley, *Electrochem. Energy Rev.* **3** (2020) 643.

[36] X. Hui, T. Songbai, and L. Li, *Mater. Res. Bull.* **42** (2007) 1301.

[37] J. Yao, Y. Ji-Li, G. Qiubo, X. Qiuying, Z. Chong, F. Tao, X. Jing, and X. Hui, *Small* **14** (2018) 1704296.

[38] J. Rong, Y. Jili, X. Qiuying, X. Jing, Z. Xiaohui, S. Shuo, Z. Teng, and X. Hui, *Energy Storage Mater.* **13** (2018) 303.

[39] X. H. Liu, L. Zhong, S. Huang, S. X. Mao, T. Zhu, and J. Y. Huang, *ACS Nano* **6** (2012) 1522.

[40] Y. Domi, H. Usui, M. Shimizu, Y. Kakimoto, and H. Sakaguchi, *ACS Appl. Mater. Inter.* **8** (2016) 7125.

[41] N. Chiodini, F. Meinardi, F. Morazzoni, A. Paleari, R. Scotti, and D. D. Martino, *J. Non-Cryst. Solids* **261** (2000) 1.

[42] W. Chang, C. Park, J. Kim, Y. Kim, G. Jeong, and H. Sohn, *Energ. Environ. Sci.* **5** (2012) 6895.

[43] J. Rohrer and K. Albe, *J. Phys. Chem. C.* **117** (2013) 18796.

[44] Y. Domi, H. Usui, A. Ando, K. Nishikawa, and H. Sakaguchi, *ACS Appl. Energy Mater.* **3** (2020) 8619.

[45] K. Ogata, S. Jeon, D. S. Ko, I. S. Jung, J. H. Kim, K. Ito, Y. Kubo, K. Takei, S. Saito, Y. H. Cho, H. Park, J. Jang, H. G. Kim, J. H. Kim, Y. S. Kim, W. Choi, M. Koh, K. Uosaki, S. G. Doo, Y. Hwang, and S. Han, *Nat. Commun.* **9** (2018) 479.

[46] K. Ogata, E. Salager, C. J. Kerr, A. E. Fraser, C. Ducati, A. J. Morris, S. Hofmann, and C. P. Grey, *Nat. Commun.* **5** (2014) 3217.

[47] K. M. Shaju, G. V. S. Rao, and B. V. R. Chowdari, *Electrochim. Acta* **48** (2002) 145.

[48] N. Yabuuchi and T. Ohzuku, *J. Power Sources* **119–121** (2003) 171.

[49] C. Zhang, F. Wang, J. Han, S. Bai, J. Tan, J. Liu, and F. Li, *Small Structures* **2** (2021) 2100009.

[50] T. Hirono, H. Usui, Y. Domi, W. Irie, T. Sawada, and H. Sakaguchi, *ACS Omega* **7** (2022) 1223.

[51] V. L. Chevrier, J. W. Zwanziger, and J. R. Dahn, *J. Alloys Compd.* **496** (2010) 25.

[52] G. Hasegawa, K. Kanamori, N. Kannari, J. Ozaki, K. Nakanishi, and T. Abe, *J. Power Sources* **318** (2016) 41.

[53] A. Kamiyama, K. Kubota, D. Igarashi, Y. Youn, Y. Takeyama, H. Ando, K. Gotoh, and S. Komaba, *Angew. Chem., Int. Ed.* **60** (2021) 5114.

[54] H. Usui, T. Sakata, M. Shimizu, and H. Sakaguchi, *Electrochemistry* **83** (10) (2015) 810.

[55] H. Usui, Y. Domi, K. Fujiwara, M. Shimizu, T. Yamamoto, T. Nohira, R. Hagiwara, and H. Sakaguchi, *ACS Energy Lett.* **2** (2017) 1139.

[56] H. Usui, Y. Domi, H. Nishida, K. Yamaguchi, R. Yamagami, and H. Sakaguchi, *ChemistrySelect* **3** (2018) 8462.

[57] H. Usui, Y. Domi, M. Shimizu, A. Imoto, K. Yamaguchi, and H. Sakaguchi, *J. Power Sources* **329** (2016) 428.

[58] H. Usui, S. Yoshioka, K. Wasada, M. Shimizu, and H. Sakaguchi, *ACS Appl. Mater. Inter.* **7** (12) (2015) 6567.

[59] H. Usui, Y. Domi, E. Iwama, H. Kurokawa, and H. Sakaguchi, *Mater. Chem. Phys.* **272** (2021) 125023.

[60] H. Usui, Y. Domi, S. Ohshima, and H. Sakaguchi, *Electrochim. Acta* **246** (2017) 280.

[61] M. Shimizu, H. Usui, and H. Sakaguchi, *J. Power Sources* **248** (2014) 378.

[62] H. Usui, Y. Domi, R. Yamagami, K. Fujiwara, H. Nishida, and H. Sakaguchi, *ACS Appl. Energy Mater.* **1** (2018) 306.

[63] H. Usui, Y. Domi, N. Takada, and H. Sakaguchi, *Cryst. Growth Des.* **21** (2021) 218.

[64] T. Hirono, H. Usui, Y. Domi, T. Nishida, W. Irie, T. Sawada, and H. Sakaguchi, *Electrochemistry* **90** (2022) 067001.

List of Publications

[1] Improvement of the Anode Properties of Lithium-Ion Batteries for SiO_x with a Third Element

T. Hirono, H. Usui, Y. Domi, W. Irie, T. Sawada, and H. Sakaguchi,

ACS Omega, **7** (2022) 1223-1231.

[2] Effect of Sn Addition on the Anode Properties of SiO_x for Lithium-Ion Batteries

T. Hirono, H. Usui, Y. Domi, T. Nishida, W. Irie, T. Sawada, and H. Sakaguchi,

Electrochemistry, **90** (2022) 067001-1-8.

[3] Effect of Sn Addition on Anode Properties of SiO_x in Sodium-Ion Batteries

T. Hirono, H. Usui, Y. Domi, W. Irie, T. Nishida, T. Sawada, and H. Sakaguchi,

Electrochemistry, **91** (2023) 017001-1-5.

Supplementary Publications